République Algérienne Démocratique et Populaire

Ministère de l'Enseignement Superieure et de la Recherche Scientifique

---

Université Echahid Hamma Lakhdar d'El-Oued

FACULTE DE TECHNOLOGIE

DEPARTEMENT DE GENIE MECANIQUE

Mémoire de fin d'étude

Présenté pour l'obtention du diplôme de

MASTER ACADEMIQUE

Domaine : Sciences et Technologies

Filière : Génie mécanique

Spécialité : Energétique et Énergies renouvelables

Thème

Performance Investigation of PV/LHP Heat Pump System

Devant le jury composé de :

Letaim Fethi	Président
Boukhari Ali.	Examinateur
MENACEUR Réda	Encadreur

Présenté par :

- CHEMSA Boudiaf
- BENHAOUA Taha

2016-2017

ACKNOWLEDGEMENTS

Foremost, we thank god for everything.

We would like to express our sincere gratitude to our academic advisor Mr Reda MENACEUR for the continuous support, patience, motivation, enthusiasm, and immense knowledge. His guidance helped us in all the time of research and writing of this thesis.

Our sincere thanks also go to Prof. Boubaker BENHAOUA and Dr. Ali CHEMSA for their encouragement, insightful comments, and wisely guidance.

We are grateful to the immense help of CDER director Ms. Rahma BESSAH and Mr Rédha YAICHE.

We would like to acknowledge the Department Mechanic, administration, professors and all classmates.

Last but not least, we would like to thank all the people who contributed in some way to the work described in this thesis.

ABSTRACT

With the widespread deployment of solar photovoltaic (PV) and thermal devices, this work aims to provide an improvement to the existing solar photovoltaic/thermal (PV/T) technologies by combining the advantages of recently proposed innovative systems. The first was a PV/loop heat pipe (LHP) that has the idea of reducing the thermal resistance between the PV layer and the thermal absorber using a coated aluminium-alloy sheet as a baseboard. The second's idea was about reducing the thermal resistance inside the PV layer via a boron Nitride doped EVA (PV Layers sealant, Ethylene-Vinyl Acetate) dedicated to PV/T systems. In addition to the use of recent accurate formula for the PV panel tilt angle keeping low solar beams' incident angle as long as possible during the day.

The overall investigation followed the basic methodology of theoretical analysis, including literature review, concept design, and full range of specialized simulation models was developed to predict the system performance with reasonable accuracy in real climatic conditions. Simulation results shown good coherence of the theoretical model with previous simulation results with significant performance improvement. Electrical and thermal efficiencies were 11.30% and 53.41%, the water temperature reached 60.8 °C in January at the region of Algiers. The research results are expected to configure feasible solutions for future PV/T technologies and encourage fabrication of such a new solar-driven heating system.

RESUME

Avec le vaste déploiement des systèmes solaires photovoltaïques (PV) et thermiques, ce travail a pour objet d'améliorer les technologies solaires photovoltaïques/thermiques existantes (PV/T) en combinant les avantages des systèmes innovants récemment proposés. Le premier est un PV/LHP qui a l'idée de réduire la résistance thermique entre le module PV et l'absorbeur thermique à l'aide d'une feuille revêtue en alliage d'aluminium comme plaque de base. L'idée du deuxième était de réduire la résistance thermique à l'intérieur du module PV via un EVA dopé au nitrure de bore (colle pour couches PV, éthylène-acétate de vinyle) dédié aux systèmes PV/T. En plus de l'utilisation d'une formule précise récente pour l'angle d'inclinaison de panneau PV, gardant l'angle d'incidence des rayons solaires bas aussi longtemps que possible pendant la journée.

L'étude a suivi la méthodologie de base d'analyse théorique, y compris l'état de l'art, la conception du système, et un paquet complet de modèles de simulation spécialisés a été développé pour prédire la performance du système avec une précision raisonnable dans les conditions climatiques réelles. Les résultats de la simulation ont montré une bonne cohérence du modèle théorique avec résultats de simulation antérieure avec une amélioration significative de la performance. L'efficacité électrique et thermique été de 11,30% et de 53,41%, la température de l'eau a atteint 60,8 °C en Janvier dans la région d'Alger. Les résultats de la recherche devraient configurer des solutions réalisables pour les futures technologies PV/T et encourager la fabrication d'un tel système autonome solaire.

TABLE OF CONTENTS

ACKNOWLEDGEMENTS

ABSTRACT

RESUME

TABLE OF CONTENTS

LIST OF FIGURES

LIST OF TABLES

ABBREVIATIONS

NOMENCLATURE

Introduction 1

I. Literature Review 3

I.1. Chapter Introduction 3

I.2. Basic Concept and Theory, Classification and Performance Evaluation Standards of PV/T Technology 3

I.2.1. Basic Concept and Theory behind PV/T Operation 3

I.2.2. Classification of PV/T Technology 6

I.3. Historical Reviews on PV/T and PV/LHP 11

I.3.1. Historical Review on PV/T 11

I.3.2. Historical Review on PV/LHP 13

I.3.3. Analysis of the Reviewed Works 15

I.4. Development of the PV/T Technology in the Master Project 17

I.5. Chapter Conclusion 18

II. Conceptual Design 19

II.1. Chapter Introduction 19

II.2. System Description and Working Principle 19

II.3. Parameters of the New PV/LHP Heat Pump System 23

II.4. Parametric Design of System Components 24

II.4.1. Glazing Cover 24

II.4.2. Al-alloy-based PV Layer 24

II.4.3. LHP with Fin Sheet 25

II.4.4. Flat-plate Heat Exchanger 27

II.4.5. Heat Pump 28

II.4.6. Insulation Material 29

II.5. Chapter Conclusion 29

III. Theoretical Analysis and Development of The Computer Simulation Models 30

III.1. Chapter Introduction 30

III.2. Analytical Model for the LHP Heat Transfer Limit 30

III.2.1. Modelling Objective for the LHP Heat Transfer Limit 30

III.2.2. Thermal Fluid Theory and the Associated Mathematical Equations of the LHP Heat Transfer Model 30

III.2.3. Algorithm for the LHP Heat Transfer Model Development and Operation 40

III.2.4. Result Discussion of LHP Heat Transfer Limit 41

III.3. Dynamic Model for the Evaluation of System Performance 46

III.3.1. Modelling Objective for the System Dynamic Performance 46

III.3.2. Thermal Fluid Theory and the Associated Mathematical Equations of the System Dynamic Model 46

III.3.3. Algorithm for the Dynamic Model Development and Operation 58

III.4. Chapter Conclusion 59

IV. Results & Findings 60

IV.1. Chapter Introduction 60

IV.2. Results and Discussion 61

IV.2.1. Temperature distribution... 61

IV.2.2. PV/LHP module’s electrical output and efficiency 62

IV.2.3. PV/LHP module’s thermal output and efficiency.. 63

IV.2.4. Cooling effectiveness & Total efficiency behavior 64

IV.2.5. Temperature Distribution Profile in Fin Sheet at Fixed Time 65

IV.2.6. Water Heat Gain and Refrigerant Mass Flow Rate... 69

IV.3. Conclusion 70

Bibliography 6071

LIST OF FIGURES

Fig. 1-1: *Established efficiency-to-temperature relationship* 5
Fig. 1-2: *Network of different solar conversion technologies* 5
Fig. 1-3: *A focused cross section of a typical PV/T module* 6
Fig. 1-4: *Cross sections of air-based PV/T modules* 8
Fig. 1-5: *Cross sections of water-based PV/T modules* 8
Fig. 1-6: *Cross-section of a PV evaporator roof panel* 9
Fig. 1-7: *Schematic of a conventional heat pipe* 10
Fig. 2-1: *Schematics of (a) the heat pump-assisted PV/LHP solar water heating system and (b) concept design of the LHP three-way Vapor-liquid separation structure* 21
Fig. 2-2: *Concept design of (a) the PV/LHP collector and (b) configuration of the PV layer* 22
Fig. 2-3: *Heat pump thermodynamic cycle in a Temperature-Entropy chart* 23
Fig. 3-1: *Schematic of the thermal and hydrodynamic couplings in the LHP* 31
Fig. 3-2: *Wick and pore parameters in the evaporator and condenser* 34
Fig. 3-3: *Flow chart for calculating the LHP heat transfer limits* 40
Fig. 3-4: *Impact of operational temperature on the heat transfer performance of the LHP* 41
Fig. 3-5: *Impact of evaporator diameter on the heat transfer performance of the LHP* 42
Fig. 3-6: *Impact of evaporator length on the heat transfer performance of the LHP* 43
Fig. 3-7: *Impact of evaporator inclination angle on the heat transfer performance of the LHP* 43
Fig. 3-8: *Impact of vapor column diameter on the heat transfer performance of the LHP* 44
Fig. 3-9: *Impact of liquid filling mass on the heat transfer performance of the LHP* 45
Fig. 3-10: *Impact of evaporator-to-condenser height difference on the heat transfer performance of the LHP* 45
Fig. 3-11: *Schematic of the transient energy balances in the system* 47
Fig. 3-12: *Grid meshing for the fin sheet along the width* 51
Fig. 3-13: *Flow chart for calculating the Dynamic Model* 58
Fig. 4-1: *The solar radiation and air temperature variation* 60
Fig. 4-2: *Wind Speed variation* 60
Fig. 4-3: *Temperature distribution in PV/LHP components* 61
Fig. 4-4: *Instantaneous Electrical Output and Efficiency Variation* 62
Fig. 4-5: *Instantaneous Thermal Output and Efficiency Variation* 63
Fig. 4-6: *Cooling effectiveness & Total efficiency behavior* 64
Fig. 4-7: *Temperature Distribution Profile in Fin Sheet at 08:00* 65
Fig. 4-8: *Temperature Distribution Profile in Fin Sheet at 12:00* 66
Fig. 4-9: *Temperature Distribution Profile in Fin Sheet at 16:00* 67
Fig. 4-10: *Temperature Distribution Profile in Fin Sheet at End 18:50* 67
Fig. 4-11: *3D Temperature Distribution Profile in Fin Sheet* 68
Fig. 4-12: *Water Heat Gain and Refrigerant Mass Flow Rate* 69

LIST OF TABLES

Table 1-1: *The characteristics comparison of different PV/T types* 11
Table 2-1: *Summary of different parameters for further characterization* 24
Table 2-2: *Alternative parameters for the glazing covers* 25
Table 2-3: *Design Parameters of the Al-alloy-based PV panel* 25
Table 2-4: *wick structure in the LHP evaporator* 26
Table 2-5: *Design parameters of the LHP operation* 27
Table 2-6: *Thermodynamic properties of water with operating temperatures* 28
Table 2-7: *Design parameters of the flat-plate heat exchanger* 29
Table 2-8: *Sample thermodynamic properties of the R134a refrigerant in the heat pump* 29
Table 2-9: *Thermal resistance of typical insulating materials* 30
Table 3-1: *Impact of wick structure on the heat transfer performance of the LHP* 42
Table 4-1: *Average Data and Results comparison* 61

ABBREVIATIONS

Al	Aluminium
BDF	Backward differentiation formula
BIPV	Building integrated photovoltaic
COP	Coefficient of performance
CPT	Cost payback time
EPBT	Energy payback time
EVA	Ethylene-vinyl acetate
FEM	Finite element method
HVAC	Heating, ventilation and air conditioning
IM	Iterative method
IPVTS	Integrated photovoltaic/thermal system
LHP	Loop heat pipe
ODE	Ordinary differential equation
OHP	Oscillating heat pipe
PDE	Partial differential equation
PV	Photovoltaic
PV/e	Photovoltaic/evaporator
PV/FPHP	Photovoltaic/flat-plate heat pipe
PV/LHP	Photovoltaic/loop heat pipe
PV-SAHP	Photovoltaic solar-assisted heat pump
PV/T	Photovoltaic/thermal
TPT	Tedlar-Polyester-Tedlar

NOMENCLATURE

A	area (m^2)
c_p	specific heat at a constant pressure (J/kg-K)
C	constant; cost
D	diameter (m)
f	solar fraction; frictional factor
F	frictional coefficient
F'	efficiency factor
F_f	standard fin efficiency
F_R	heat removal factor
F_{th}	thermal efficiency factor
g	gravity acceleration (m/s^2)
h	heat transfer coefficient (W/m-K)
h_c	convective heat transfer coefficient (W/m-K)
h_{fg}	latent heat of vaporization (J/kg)
h_m	hour angle (rad)
h_R	radiative heat transfer coefficient (W/m-K)
H	thermal enthalpies (kJ/kg)
H_h	height of heat exchanger plate (m)
I	solar radiation intensity (W/m^2)
k	thermal conductivity (W/m^2-K)
K	extinction coefficient of glass cover
K_p	wick permeability (m^2)
L	length (m)
L_m	local latitude
φ	inclination angle

Subscripts

a	
abs	air
aG	absorption
b	axial hydrostatic pressure
bos	baseboard; bubbles
BL	balance of system
c	boiling limit
c,max	cover; collecting; compressor
c,r	maximum capillary
c,t	cross area of refrigerant
c_1	condensation energy
c_2	internal cover sheet
CL	external cover sheet
e	capillary limit
ei	electricity; evaporator
el	electrical insulation
en	electrical
exp	net electricity
EL	experiment
f	entrainment limit
fc	fin sheet; groove fin
fe	center of fin sheet
fl	edge of fin sheet
fs	filled liquid
FL	insulation around fin sheet

m	mass flow rate (kg/s); molecular	g	groove
M	mass (kg); Mach number	g,pv	glass of PV limitation
n	mesh number; iteration number	G	gravity
n_g	ratio of refraction index	hp	heat pipe
N	number	hp,in	heat pipe inner wall
Nu	Nusselt number	hp,o	heat pipe outer wall
P	pressure (Pa)	hp,w	heat pipe wall
P_o	measured output power (W)	hx	heat exchanger
Pr	Prandtl number	hx,hp	heat exchanger to heat pipe
q	energy rate per unit area (W/m^2)	hx,in	heat exchanger inner
Q	energy rate (W)	hx,o	heat exchanger outer
r	thermal resistance per area (m^2-K/W)	hx,r	refrigerant within heat exchanger
$r_{h,s}$	hydraulic radius of wick pore (m)	i	differential length node; inlet; inner layer
r_e	effective capillary radius (m)	k	differential time node
R	thermal resistance (K/W)	l	liquid
Ra	Rayleigh number	lf	liquid film
Re	Reynolds number	L	loss
R_0	universal gas constant (kJ/kmol-K)	m	mean; module
R_v	vapour constant (kJ/kg-K)	mtl	replacing materials
t	time (s)	o	overall; outer layer
T	temperature (K)	out	outlet
T_{su}	solar temperature at 6000 K	p	PV; pressure
U	heat loss coefficient (W/m^2-K)	PV/T	PV/thermal
V	velocity (m/s)	r	refrigerant
W	width (m)	rc	reference temperature
x	width parameter; parameter to the liquid filling mass	r,e	refrigerant evaporator
x_r	refrigerant saturation rate	r,l	liquid refrigerant
		r,m	mean refrigerant

Greek

α	absorption ratio; width-to-length
β_p	PV packing factor
β_{PV}	efficiency temperature coefficient
γ	vapor specific heat ratio
$r_{\|\|}$	parallel components of unpolarized radiation for smooth surfaces
$r_{\perp}$	perpendicular components of unpolarized radiation for smooth surfaces
δ	thickness (m)
δ_m	declination angle (rad)
ε	emissivity; porosity; resistance
E	energy output
ξ	exergetic efficiency
Z	reduction of greenhouse gas
η	energetic efficiency
θ	collector slope (rad)
θ_e	contact angle of evaporator (rad)
θ_1	incidence angle (rad)
θ_2	refraction angle of direct solar beam (rad)
μ	dynamic viscosity (kg/m-s)
ν	kinematic viscosity (m^2/s)
ρ	density (kg/m^3)
σ	Stefan–Boltzmann constant ; surface tension coefficient (N/m)
Σ	embodied energy
τ	transmittance
$\tau_{c,a}$	transmittance for absorption

s	radial hydrostatic pressure
s,g	solid groove
sim	simulation
s,ms	solid mesh screen
s,sp	solid sintered powder
SL	sonic limit
th	thermal
u	useful
v	vapor
v,e	vapor core in evaporator
vt	vapor in three-way fitting
vtl	vapor transportation line
vtl,in	inner vapor line
vtl,o	outer vapor line
VL	viscous limit
w	water
wi	wick
wi,g	groove wick
wi,ms	mesh screen wick
wi,sp	sintered powder wick
wm	working medium
ws	insulation of water tank
ws,in	inner tank insulation
ws,o	outer tank insulation

Introduction

Introduction

The PV is currently the most popular solar power device that has the temperature-dependent solar electrical output. It is understood that increasing temperature of PV cells by 1 °C would lead to 0.5% reduction in the solar electrical efficiency for the crystalline silicon cells and around 0.25% for the amorphous silicon cells [11]. To control the cell temperature, several measures were applied to remove the accumulated heat from the back surface of PV modules and further to make advanced utilization of the removed heat. This approach, known as the PV/Thermal (PV/T) technology, enables the dual solar collecting functions in one module for output of both electricity and heat. As a kind of PV/T systems the PV/heat pipe hybrid technology concluded by several recent studies as the most compromising system in term of price/efficiency and has the potential to overcome persisting PV/T difficulties.

Gang et al. [37] carried out a numerical and experimental study on a heat pipe PV/T system A novel heat-pipe photovoltaic/thermal system was designed and constructed by the authors. They found that the daily thermal and electrical efficiencies of the photovoltaic/ heat-pipe system were 41.9% and 9.4%, respectively, while the average heat and electrical gains were 276.9 and 62.3 W/m2, respectively. Zhang et al [38] in Design, fabrication and experimental study of a solar photovoltaic/loop-heat-pipe based heat pump system, and an investigation into the dynamic performance of a novel solar photovoltaic/loop-heat-pipe (PV/LHP) heat pump system. a novel coated aluminium-alloy (Al-alloy) sheet was applied as the baseboard of PV cells for enhanced heat dissipation to the surroundings. During the outdoor testing, the mean daily electrical, thermal and overall energetic and exergetic efficiencies of the PV/LHP module were measured at 9.13%, 39.25%, 48.37% and 15.02% respectively.

Application of the loop heat pipe (LHP) in the heat-pipe based PV/T system may have potential to further improve the performance of such a system. LHP is regarded as a special type of heat pipe and is famous for large capacity of remote and passive heat transfer by circulating the working fluid in a closed loop. It has been already widely utilized in thermal controls of satellites, spacecraft, electronics, cooling/heating systems, while its application in solar energy system is proposed recently [11].

According to previous PV/LHP works, a novel coated Al-Alloy sheet used as baseboard to replace the conventional TPT baseboard in order to enhance heat transfer from PV module to fin sheet (thermal absorber) and then to LHP, but still relatively high thermal resistance beneath the PV layer owned to the moderate EVA thermal conductivity which means a considerable part of the heat will always be trapped inside the PV module, in the other hand, other works proposed a Boron Nitride doped EVA dedicated for PV/T systems in order to ensure a good thermal conductivity within the PV module, but even so, still low profitability of this novel technique if used with conventional TPT baseboard due to its low thermal conductivity. The objective of this work, besides of using accurately calculated tilt angle for better profitability of solar radiation, is to use the enhancement of both innovative ideas in one system gaining a much better thermal conduction through the whole system and a quick heat evacuation from PV module which definitely will improve the system's performance. The research results will contribute a certain added value to the development of PV/T technology and encourage to further work of building and experiment the proposed system.

The present work will be divided as follow:

Introduction: this briefly describes the research background, significance, objectives, research concept, methodology and novelty.

Chapter I – Literature review: this involves a review of the existing PV/T technologies, including basic theory, research methodology, PV/T and PV/LHP history, and analysis of the reviewed works.

Chapter II – Conceptual design: this describes the basic working principle of the system and creates a schematic design for key components. Structures, materials, geometric and operating conditions of the system are recommended for the further input of theoretical simulation.

Chapter III – III. Theoretical Analysis and Development of The Computer Simulation Models: this develops a group of dedicated computer simulation models for the LHP device and the whole system by analyzing the fundamental equations of the energy balances, solar transmittance, heat transfer, fluid flow and photovoltaic generation.

Chapter IV – Results & Findings: this will discuss the results of the simulation of the system in real climatic conditions, comparison of the results with previously published experiment of similar system and detailed interpretation of the obtained plots followed by a conclusion and perspective.

Chapter I:

Literature Review

I. Literature Review

I.1. Chapter Introduction

This chapter will present a review of R&D progress and history of PV/T and PV/heat pipes technologies. The major objectives are as follow:

1) Present the idea of PV/T technology and the its theory.
2) Show a comprehensive literature review.
3) Analyze the review in the categories of PV/T type.
4) Identify the main features, research highlights and current technical barriers of different PV/T technologies.

I.2. Basic Concept and Theory, Classification and Performance Evaluation Standards of PV/T Technology

I.2.1. Basic Concept and Theory behind PV/T Operation

As known, PV cells are solar electricity-generators. Their solar efficiency is a critical parameter for justifying their overall performance, which is highly dependent on the cells' quality of materials and its operating temperature. Generally, PV electrical efficiency is in the range of 6% to 18%, measured at the nominal operating temperature (NOCT) (0.8 kW/m^2 of solar radiation, 20 °C of ambient temperature, and 1 m/s of air velocity) [1]. It is well known that the electrical efficiency of a PV cell decreases with an increase in its operating temperature, as shown in **Fig. 1-1**. The photon of longer wavelengths striking the solar cells generates a lot of heat than that of electron-hole pairs. Increasing the temperature of a PV cell by 1 degC leads to 0.4% to 0.5% reduction in the electrical efficiency for crystalline silicon cell [2, 3] and 0.25% for amorphous silicon (a-Si) cell [4].

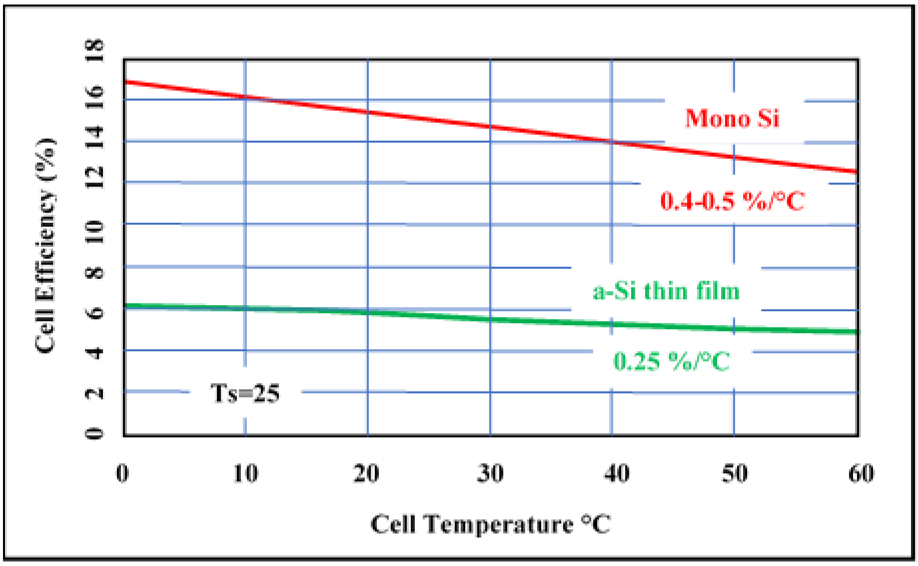

Fig. 1-1: *Established efficiency-to-temperature relationship*

A Photovoltaic/Thermal hybrid (abbreviated as PV/T) collector is the combination of a PV collector on top and a thermal collector at the bottom. The idea behind combining these two is to increase PV electrical efficiency and make full utilization of solar radiation by circulating a fluid, which will extract heat from the concealed PV surface and collect the residual heat effectively. Furthermore, in cases where heating is required, extracted heat from the PV modules serves as a second benefit along with the increased performance of the PV module. Thus, this hybrid solar collector can obtain an enhanced overall solar efficiency and provide an effective method for the utilization of solar energy [5]. The PV/T device represents a new direction for renewable heating and power cogeneration.

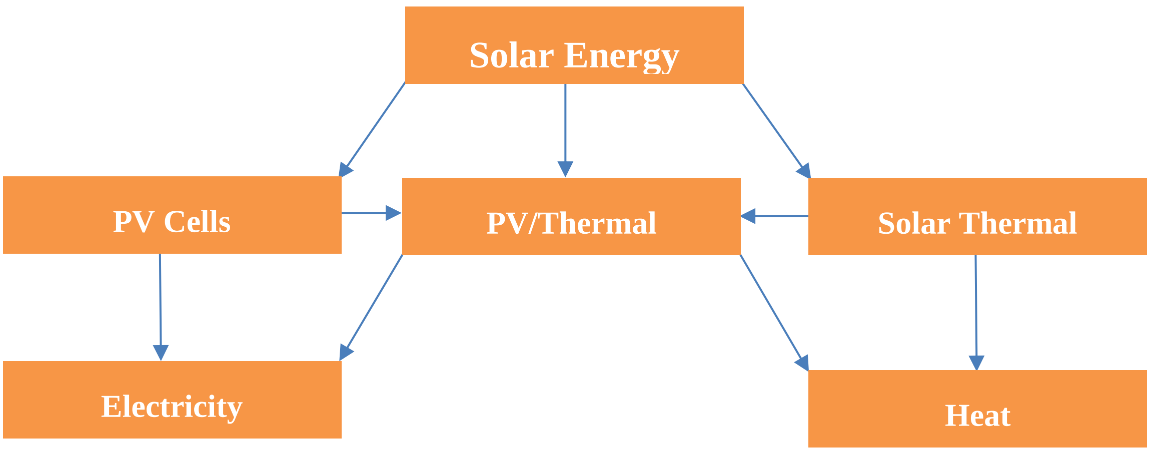

Fig. 1-2: *Network of different solar conversion technologies*

Generally, a PVT module is a sandwiched structure of several layers namely: flat-plate clear glazing as the top layer; a layer of photovoltaic cells or a commercial PV lamination beneath the cover with a small air gap; a thermal absorber closely adhered to the PV layer; and a thermally insulated layer located immediately below the flow channels. All the layers are fixed into a frame using adequate clamps and connections. **Fig. 1-3** displays a schematic of a typical PV/T module structure.

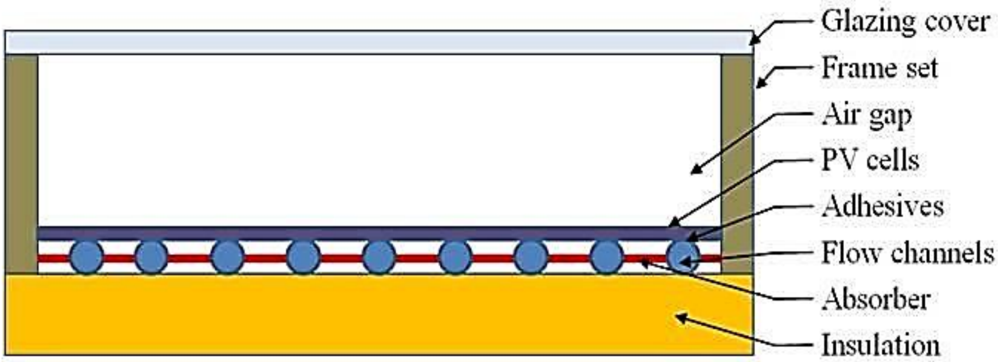

Fig. 1-3: *A focused cross section of a typical PV/T module*

The overall efficiency is the sum of the collector's thermal efficiency and the PV electrical efficiency.

$$\eta_0 = \eta_{th} + \eta_e \qquad [1-1]$$

where, η_o is the overall efficiency; η_{th} and η_e represent the thermal and the electrical efficiencies respectively.

(1) Thermal Efficiency

Useful thermal energy to the overall incident irradiation.

$$\eta_{th} = \frac{Q_u}{I\,A_c} \qquad [1-2]$$

where, Q_u is the useful thermal energy (W); I is the incident irradiation (W/m^2) and A_c is the collecting area of the module (m^2).

The heat gathered by the flat-plate PV/T collector could either be given as

$$Q_u = mc_p(T_{out} - T_i) \qquad [1-3]$$

where, m is the mass flow rate of working medium (kg/s); c_p is the specific heat capacity at a constant pressure of working medium (J/kg-K); T_{out} and T_i are the temperatures of the module outlet and inlet (K).

Or simply, the difference in the absorbed solar radiation, heat loss and electrical energy produced

$$Q_u = A_c\left[I(\tau\alpha) - U_L\left(T_{p,m} - T_a\right) - q_e\right] \qquad [1-4]$$

where, $\tau\alpha$ is the transmittance-absorption coefficient of glazing cover; U_L is the heat loss coefficient (W/m^2-K); $T_{p,m}$ and T_a are the temperatures of the PV module and ambient (K); q_e is module electrical output per unit area (W/m^2).

(2) Electrical Efficiency

The electrical efficiency of a PV module decreases with an increase in the cell's working temperature [6]

$$\eta_e = \eta_{rc}\left[1 - \beta_{PV}\left(T_p - T_{rc}\right)\right] \qquad [1-5]$$

where, η_{rc} is the initial electrical efficiency at reference temperature; β_{PV} is the cell efficiency temperature coefficient (1/K); T_p and T_{rc} are respectively the PV cell temperature and its reference temperature (K).

Alternatively, the electrical efficiency (η_e) of a PV module is represented as the generated electrical energy, Q_e (W), to the overall incident solar radiation

$$\eta_e = \frac{Q_e}{I A_c} \qquad [1-6]$$

I.2.2. Classification of PV/T Technology

PV/T modules can be grouped into several classes depending on their configuration, cooling fluid, temperature level and function. From the cooling fluid point of view, there are currently four types of PV/T collector, which are the devices developed using air, water, refrigerants, and heat pipes.

(1) Air-based PV/T Technology

Usually, this PV/T system is designed for end users who have a demand for hot air, space heating, agricultural/herb drying or increased ventilation. For this module type, air can be delivered from above, below or on both sides of the PV absorber, as shown in **Fig. 1-4**.

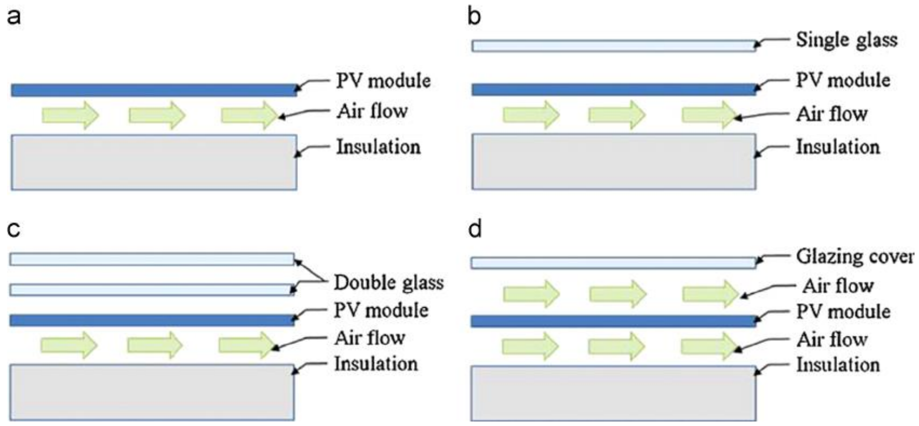

Fig. 1-4: *Cross sections of air-based PV/T modules* [7]

(2) Water-based PV/T Technology

It has the same structure to a conventional flat-plate solar collector. The absorber is attained with numerous PV cells that are either connected in a series or parallel. They are fixed under serpentine or a series of parallel tubes. Water is forced to flow across the tubes and, if the water temperature remains low, the PV cells will be cooled, thus leading to increased electrical efficiency. Zondag et al. [8] addressed several water flow patterns for PV/T collectors: sheet and tube, channel, free flow and two absorber types, which are shown schematically in **Fig. 1-5**.

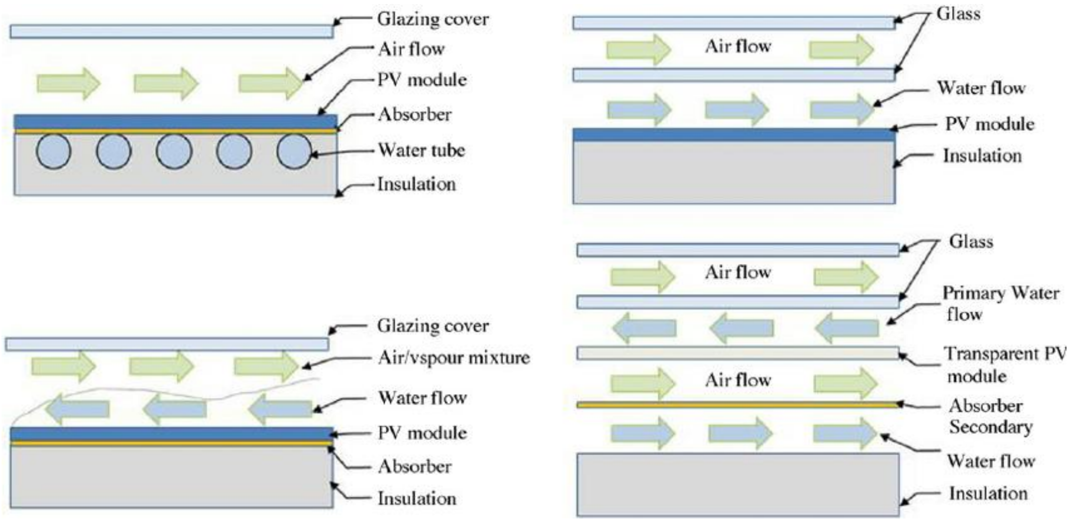

Fig. 1-5: *Cross sections of water-based PV/T modules* [7]

(3) Refrigerant-based PV/T Technology

Recent study has suggested a novel concept of a PV/T module for heat pump application. This solar technology lays direct expansion evaporation coils underneath the PV modules, which allows a refrigerant to be evaporated when passing through the modules. In this way, the coils act as the evaporation sector of the heat pump, which allows the refrigerant to evaporate at a remarkably low temperature. As a result, the PV cells are cooled to a similar low temperature. The compressor of the heat pump increases the pressure of the vapor generated from the panels and delivers it to the condenser to provide heating. **Fig. 1-6** gives a cross-sectional view of a glazed PV evaporator (PV/e) roof panel [9].

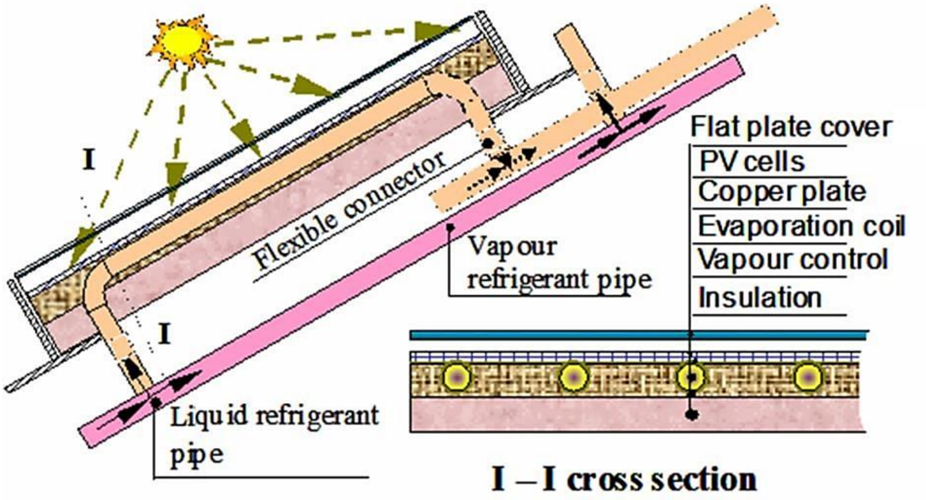

Fig. 1-6: *Cross-section of a PV evaporator roof panel*

(4) Heat-pipe-based PV/T Technology

They are considered as the most efficient heat transfer mechanism that combines the principles of both thermal conductivity and phase transition. A typical heat pipe, as indicated in **Fig. 1-7** [10], consists of three sections: an evaporation section (evaporator), an adiabatic section and a condensation section (condenser), and provides an ideal solution for heat removal and transmission.

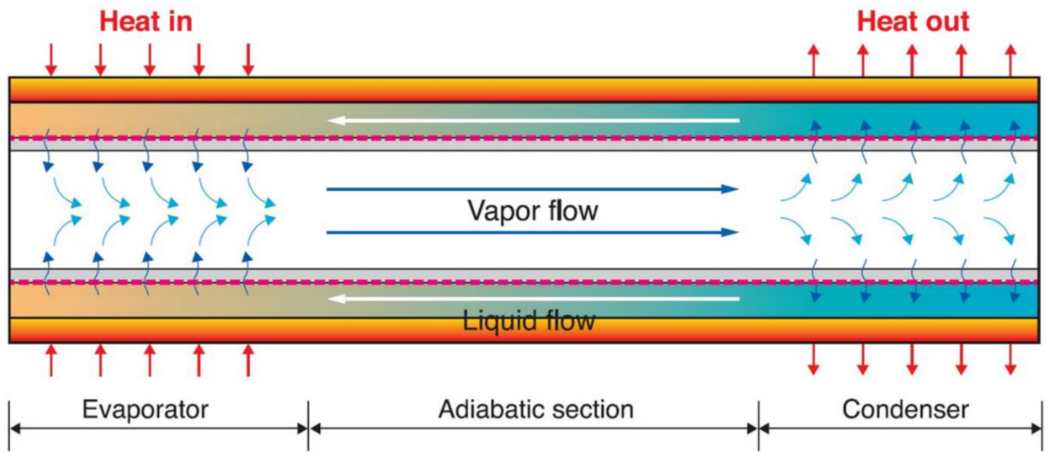

Fig. 1-7: *Schematic of a conventional heat pipe*

Many studies were conducted on PV/heat pipe based system achieved remarkable results. The most recently Xingxing Zhang et al. [11] proposed a novel solar photovoltaic/loop-heat-pipe (PV/LHP) module-based heat pump system designed and fabricated for both electricity and hot water generation. A novel top-positioned three-way tube (the vapor-liquid separation structure) as a system of separation between vapor and liquid return in the transportation line used and a coated aluminium-alloy (Al-alloy) sheet was applied as the baseboard of PV cells for enhanced heat dissipation to the surroundings. The whole prototype system was subsequently evaluated in outdoor weather conditions throughout a consecutive period for about one week. PV efficiency was about 9.18%, nearly 0.26% higher than the TPT based type. fluid.

(5) Technical Characteristics of Currently Available PV/T Types

A comparison between the four PV/T types was made in terms of their technical characteristics. The overall module efficiencies for different PV/T types were calculated with the same external solar/weather conditions (i.e., weather conditions on 22nd, December in the Midwestern area of the UK) and operational conditions (i.e., 0.01 kg/m2-s of mass flow rate, 10% of initial PV efficiency). The calculation models used were as follows: (1) an indoor-simulator (IS) model for air-based PV/T [12]; (2) an integrated PV/T system (IPVTS) model for water-based PV/T [13]; (3) a PV solar-assisted heat pump (PV-SAHP) model for refrigerant-based PV/T [14]; and (4) a PV/flat-plate heat pipe (PV/FPHP) model for heat-pipe-based PV/T [15]. **Table 1-1** gives a specific description of the characterized results.

Table 1-1: *The characteristics comparison of different PV/T types*

PV/T models	Efficiency	Advantage	Disadvantages
IS model for air- based PV/T type [12]	24%–47%	- Low cost - Simple structure	- Low thermal mass - Large air volume - Poor thermal removal effectiveness - High heat loss
IPVTS model for water-based PV/T type [13]	33%–59%	- Low cost - Direct contribution - High thermal mass - Low flow volume	- Still high PV temperature - Unstable heat removal effectiveness - Complex structure - Possible pipe freezing
PV-SAHP model for refrigerant-based PV/T type [14]	56%–74%	- Low PV temperature - Stable performance - High efficiency - Effective heat removal	- Risk of leakage - Unbalanced liquid distribution - High cost - Difficult to operate
PV/FPHP model for heat-pipe-based PV/T type [15]	42%–68%	- Low PV temperature - Stable performance - High solar efficiency - Effective heat removal - Reduced power input	- High cost - Risk of damage - Complex structure

I.3. Historical Reviews on PV/T and PV/LHP

I.3.1. Historical Review on PV/T

Several pieces of research were done to study the performance of different PV/T configurations, optimize their geometric sizes and recommend the most appropriate operational parameters. As a result, a sufficient quantity of experience has been obtained and this is indicated as follow.

Hendrie [16] developed a theoretical model for the flat plate PVT solar collectors and by using the model. He concluded that the air and liquid based units obtained respectively thermal and electrical efficiencies of 40.4% and 32.9% .

Cox and Raghuraman [17] explored several design features of air based flat-plate PVT collectors to determine their effectiveness based on a computer simulation. They found that air based PVT types are usually less efficient than the liquid ones, due to low PV cell packing factor, low solar absorption, high infrared emittance and low absorber to air heat transfer coefficient.

Huang et al. [18] studied an integrated photovoltaic–thermal system (IPVTS) set-up. The tested results showed that the solar PVT collector made of a corrugated polycarbonate panel can obtain a primary-energy saving efficiency of about 61.3%, while the temperatures difference between the tank water the PV module was around 4 1C.

Bergene and Lovvik [19] developed a PVT mathematical. The model was based on analysis of energy transfers including conduction, convection and radiation initiated by Duffie and Beckman and the outcome of model operation suggested that the overall efficiency of PVT collectors are in the range 60–80% [20].

Grag and Agarwal [21] proposed a simulation model to examine the output of the design and operational parameters of a PV/T air heating system. It was found that PVT air heating system largely depended on the its design temperatures as the extra glass cover might lead to the increased transmission losses and beyond some critical point the single-glass cover can collect more heat than double glass does.

Sopian et al. [22] suggested the steady-state models to analyze the performance of both single and double-pass PV/T air collectors. They concluded that the double-pass photovoltaic thermal solar collector produces better performance than the single-pass module at a normal operational mass flow rate range.

De Vries and Zondag et al. [23–25] carried out testing of a PVT solar boiler with a water storage tank in the Dutch and found that the covered sheet-and-tube system was the most promising PVT concept for tap water heating. This PVT system could achieve annual average solar efficiencies of between 34% and 39% for the covered designs, and 24% for the uncovered design.

Kalogirou [26] carried out the modelling and simulation of the performance of a hybrid PVT solar water. The results showed that the hybrid system increases the mean annual efficiency of the PV solar water system from 2.8% to 7.7% and in addition covers 49% of the hot water needs in a house, thus increasing the mean annual efficiency to 31.7%.

Jones and Underwood [27] have studied the temperature profile of photovoltaic (PV) module in a non-steady state condition with respect to time. They performed experiments for clear as well cloudy day condition and observed that the PV module temperature varies between 300 and 325 K (27–52 1C) for an ambient air temperature of 297.5 K (24.5 1C).

Huang et al. [28] have studied experimentally the unglazed integrated photovoltaic and thermal solar system (IPVTS) for water heating under natural mode of operation. They observed that the primary energy saving efficiency of IPVTS exceeds 0.60 which is higher than that for a conventional solar water heater or pure PV system.

Kalogirou [29] has studied the monthly performance of unglazed hybrid PVT system under forced mode of operation for climatic condition of Southern Cyprus and observed an increase of the mean annual efficiency of PV solar system from 2.8 to 7.7% with thermal efficiency of 49%, respectively.

Sandnes and Rekstad [30] have noticed the behavior of a combined photovoltaic thermal (PVT) collector which was constructed by pasting single-crystal silicon cells onto a black plastic solar heat absorber (unglazed PVT system). They recommended that the combined PVT concept must be used for low temperature thermal application for increasing the electrical efficiency of PV system, e.g., space heating of a building.

Sandnes and Rekstad [31] used a polymer solar heat collector, combined with single-crystal silicon PV cell to build a PVT unit . They found out that pasting solar cells onto the absorbing surface can reduce the solar energy absorbed by the panel. Further there is an increased heat transfer resistance at the surface of absorber.

Chow [32] has carried out the analysis of PV/T water collector with single glazing in a transient condition. The tube underneath flat plate with metallic bond collector was used. He noticed that photovoltaic conversion efficiency at the reduced temperature is increased by 2% at mass flow rate of 0.01 kg/s for 10,000 W/m^2K plate to bond heat transfer coefficient. An additional thermal efficiency of 60% was also obtained.

Tiwari and Sodha [33] developed a thermal model for an integrated photovoltaic and thermal solar collector (IPVTS) system and compared it with the model for a conventional solar water heater by Huang et al. The simulations predicted a daily primary energy saving efficiency of around 58%, which was in good agreement with the experimental value (61.3%) obtained by Huang et al.

I.3.2. Historical Review on PV/LHP

A heat pipe is a heat-transfer device that combines the principles of both thermal conductivity and phase transition to efficiently manage the transfer of heat between two solid interfaces [34]. The original heat pipe operating principle was developed by Richard S. Gaugler of the General Motors Corporation in 1942. Modern heat pipe technology was originated from the Los Alamos Scientific Laboratory by George Grover in 1963. Advanced Cooling Technologies' Yale Eastman (currently a Director of ACT), a few years later describes the theory and history of the heat pipe technology in an article published in Scientific American, May 1968. Since then, heat pipe technology has progressed from cooling vacuum tubes to being applied on the CPU chip of modern lap top computers. Heat pipes are even cooling satellites electronics in zero gravity orbit. Heat pipes are highly efficient conductors of heat and can transport, in some cases, 1000's times better than a solid copper conductor [35].

A loop heat pipe (LHP) is a two-phase heat transfer device that uses capillary action to remove heat from a source and passively move it to a condenser or radiator. LHPs are similar to heat pipes but have the advantage of being able to provide reliable operation over long distance and the ability to operate against gravity. They can transport a large heat load over a long distance with a small temperature difference. Different designs of LHPs ranging from powerful, large size LHPs to miniature LHPs. Loop heat pipes were patented in USSR in 1974 by Yury F. Gerasimov and Yury F. Maydanik, all of the former Soviet Union. The patent for LHPs was filed in the USA in 1982. [36].

Gang et al. [37] performed a numerical and experimental study on a heat pipe PV/T system. A novel heat-pipe photovoltaic/thermal system was designed and constructed by the authors. A dynamic model was developed to predict the performances of the heat-pipe photovoltaic/thermal system. He also conducted experiments to validate results obtained for the simulation. He found that the daily thermal and electrical efficiencies of the heat-pipe photovoltaic/thermal system were 41.9% and 9.4%, respectively, while the average heat and electrical gains were 276.9 and 62.3 W/m2, respectively.

Zhang et al [38] in Design, fabrication and experimental study of a solar photovoltaic/loop-heat-pipe based heat pump system novel solar photovoltaic/loop-heat-pipe (PV/LHP) module-based heat pump system was designed and fabricated for both electricity and hot water generation. A coated aluminium-alloy (Al-alloy) sheet was applied as the baseboard of PV cells for enhanced heat dissipation to the surroundings, which was characterized by a series of laboratory-controlled conditions over the conventional Tedlar–Polyester–Tedlar (TPT) baseboard. The whole prototype system was subsequently evaluated in outdoor weather conditions throughout a consecutive period for about one week. Given the specific indoor testing conditions, temperature of the Al-alloy based PV cells was observed at about 62.4 °C, which was 5.2 °C lower than that of the TPT based PV cells, and its corresponding PV efficiency was about 9.18%, nearly 0.26% higher than the TPT based type. During the outdoor testing, the mean daily electrical, thermal and overall energetic and exergetic efficiencies of the PV/LHP module were measured at 9.13%, 39.25%, 48.37% and 15.02% respectively. He found that the basic-thermal system performance coefficient (COP_{th}) was at 5.51 and the advanced system performance coefficient ($COP_{PV/T}$) was nearly 8.71.

Zhang et al [11] carried out an investigation into the dynamic performance of a novel solar photovoltaic/loop-heat-pipe (PV/LHP) heat pump system for possible use in space heating or hot water generation. The methods used include theoretical computer simulation, experimental verification, analysis and comparison. The research results indicated that under the testing outdoor conditions, the mean daily electrical, thermal and overall energetic and exergetic efficiencies of the PV/LHP module were 9.13%, 39.25%, 48.37% and 15.02% respectively, and the average values of COP_{th} and $COP_{PV/T}$ were 5.51 and 8.71. The PV/LHP module was found to achieve 3–5% higher solar exergetic efficiency than standard PV systems and about 7% higher overall solar energetic efficiency than the independent solar collector. Compared to the conventional solar/air heat pump systems, the PV/LHP heat pump system could achieve a COP around 1.5–4 times that for the conventional systems. He concluded that the computer model is able to achieve a reasonable accuracy in predicting the system's dynamic performance.

Most recently, Rittidech et al. [39] in a Numerical for Predicted Efficiency of a Solar Collector Installed Heat Pipe used the mathematical model for predicted performance of a solar collector installed heat pipe system and comparison results between mathematical model and experimental data. Their comparison results between mathematical model and experimental data showed that the model was able to yield satisfactory predictions. They claim that the results of heat transfer rate and efficiency from mathematical model and experimental data of the solar collector installed heat pipe system were similar trend.

I.3.3. Analysis of the Reviewed Works

The research falls into four type categories: (1) air-based PV/T; (2) water-based PV/T; (3) refrigerant-based PV/T; and (4) heat-pipe-based PV/T technology. The air- and water-based types are relatively mature and have already been used in practical projects. The refrigerant- and heat-pipe-based systems are still at the research/laboratory stage and some technical/economic barriers remain.

(1) Air-based PV/T Technology

It has been developed into commercial units and used in many engineering practices. A typical air-based PV/T type can achieve up to 8% electrical efficiency and 39% thermal efficiency [12]. Its performance depend strongly upon air flow velocity and temperature. The main problem with the air-based system lies in its relatively poor heat removal effectiveness, related to the low thermodynamic properties of air, such as density, specific heat capacity and thermal conductivity.

(2) Water-based PV/T Technology

Water-based PV/T is the second common solar thermal and power cogeneration device, and has gained in practical use over recent years. The performance of water-based PV/T vary with the water temperature, flow rate, water flow channel geometry and sizes and PV type, as well as external climatic conditions. A typical water-based PV/T type can achieve up to 9.5% electrical and 50% thermal efficiency [13]. Its performance is largely dependent upon water temperature, flow rate, water flow channel geometry, PV type, and external climatic conditions.

In comparison with an air-based PV/T type, a water-based PV/T system could enhance the electrical efficiency of PV modules and, therefore, increase solar heat energy utilization. However, the improvement is limited due to some inherent technical difficulties. Firstly, the heat removal effectiveness of water is poor in practice as the water continuously rises in temperature over the operating period and fails to improve the solar efficiency when operating at a high-water temperature; secondly, additional back-up heating devices (to achieve the required water temperature) would increase the complexity of the system and reduce its efficiency.

(3) Refrigerant-based PV/T Technology

Refrigerant-based PV/T is the recent evolving technology. Researches shown that this system could improve the solar utilization rate significantly over the air-based and water-based and, therefore, has the potential to replace the two former systems in the future. The system usually operates in conjunction with a heat pump, and its performance is justified by the electrical and thermal efficiencies of the PV/T modules and the COP of the PV/T heat pump system. These parameters (efficiencies and COP) vary with the flow rate of the refrigerant, its preset evaporation and condensation temperature/pressure, flow channels, geometric sizes, PV type and external climatic conditions. A typical refrigerant-based PV/T type can achieve up to 10% electrical and 65% thermal efficiency [14].

In comparison with air-/water-based systems, a refrigerant-based system could significantly improve the electrical efficiency of PV cells and increase solar heat energy utilization. This initiative represents a step forward in PV cooling technology but its practicality still faces many challenges. For example, the refrigerant piping cycle needs a perfect seal in order to maintain various pressures in different sections so that it prevents air from being sucked into the system during operation. Which is very difficult to achieve owing to the large number of welding joints. There are also high risks of refrigerant leakage and the problem of achieving balanced refrigerant distribution across the multiple coils installed in a large PV panel area is technically difficult.

(4) Heat-pipe-based PV/T Technology

Heat-pipe-based PV/T is also a relatively new technology and research into this subject is very limited. To date, flat-plate and oscillating heat pipes were studied for possible use in PV cooling and the results shows that heat pipes can have the potential to overcome problems existing in a refrigerant-based system. e.g., the possible leakage of refrigerant, an imbalance in the distribution of refrigerant flow, and the difficulty of retaining pressurization or depressurization states in different parts of the system.

This system usually operates in conjunction with a heat pump or a heating cycle, and its performance is justified by the electrical and thermal efficiencies of the PV/T module and the heat pipe heat transfer capacity. These performance parameters vary with the structure/material and vacuum degree of the heat pipe, the type of heat pipe working fluid, the temperature and flow rate of the secondary fluid, PV type and external climatic conditions. In general, a typical heat-pipe-based PV/T type [15] can achieve up 10% electrical and 58% thermal efficiency.

In comparison with a refrigerant-based system, a heat-pipe-based system could achieve an equivalent performance if the heat pipes operate at an adequate temperature. This system may overcome the difficulties that exist in a refrigerant-based system and become the next generation of technology for removing heat from PV cells and effectively utilizing this part of the heat. However, this system type also has some disadvantages that require further resolution, e.g., the high cost of heat pipes and reliable control of heat pipe performance.

I.4. Development of the PV/T Technology in the Master Project

In summary, in accordance with the previous research results and future potential opportunities in the development of PV/T technology, this Master project would address the following aspects: (1) reducing the thermal resistance between the PV panel and the thermal absorber through application of a coated Al-alloy sheet as the PV baseboard [11] and using thermally enhanced EVA sealant [50]; (2) using a recently developed LHP as the thermal absorber [11]; (3) developing a full range of computer simulation models, including initial concept design; and (4) investigating the PV/LHP technology real local climatic conditions (Bouzerreah, Algiers – Algeria). These works were intended to achieve the systematic development of a new PV/T technology and cover some of the points missing in the previous research. Xingxing Zhang et al. [11] used a novel coated Al-Alloy sheet as baseboard to enhance heat transfer from PV module to fin sheet (thermal absorber) then to LHP, but with very low EVA thermal conductivity which means a considerable part of the heat will always remain trapped inside the PV module, in the other hand, J. Allan et al. [50] proposed a Boron Nitride doped EVA in order to ensure a good thermal conductivity within the PV module, but still low conductivity through TPT baseboard persists, so it is clearly wise to use the enhancement of both innovative idea in one system gaining a much better thermal conduction through the whole system and a quick heat evacuation from PV module. The research results will contribute a certain added value to the development of PV/T technology.

I.5. Chapter Conclusion

A review of the R&D works has been carried out in this chapter. The results of the work helped to understand the current status of PV/T technical development, identify potential difficulties and barriers remaining in this sector, develop potential research topics/directions to improve the performance of PV/T technology, establish associated strategic plans.

Although numerous pieces of research have been carried out in the field of PV/T technology, the industry still faces various inherent technical challenges, such as inefficient heat removal effectiveness, increasing temperature of the working fluid, potential freezing, risk of fluid leakage, and an imbalance in liquid distribution. To overcome these technical barriers, opportunities for further development of PV/T technology have been discussed, including (1) reducing thermal resistance inside PV module, between the PV module and thermal absorber; (2) developing a new heat-pipe-based thermal absorber; (3) developing a full range of simulation models; (4) evaluating system performance in real climate conditions.

The review results helped to (1) identify the technical barriers existing in current PV/T technology, (2) establish a scientific methodology for the PV/T research, (3) propose new research opportunities, and (4) build the research direction for subsequent chapters.

Chapter II:

Conceptual Design

II. Conceptual Design

II.1. Chapter Introduction

This chapter describes the new PV/T concept for hot water generation by incorporating a new doped ethylene-vinyl acetate sealant (EVA) with particles of Boron Nitride (BN 60% w/w) to glue PV layers especially for PV/T system (enhanced EVA thermal conductivity from 0.23 to 2.85 W/m.K) [50], PV coated Al-alloy sheet, an innovative LHP device and a heat pump [11]. It is intended to complete the following tasks:

(1) Present the sketch drawings of the system components.

(2) Describe the working principle of the whole system.

(3) Identify the heat-transfer requirement of LHP absorber for further design and simulation as well as other several parameters relating to the system performance, including design (structure, geometry and materials), operating and external parameters.

(4) Provide a parametric design of the different system components for further theoretical analysis.

II.2. System Description and Working Principle

The PV/LHP heat pump water heating system is shown in **Fig. 2-1 (a)**. The system comprises a modular PV/LHP collector (entitled ‘PV/LHP module’), an electricity control/storage unit, fluid vapor/liquid transportation lines, a flat-plate heat exchanger acting as the condenser for the LHP and the evaporator of the heat pump, a hot water tank, a compressor, a coil-type condenser embedded into the water tank and an expansion valve. The LHP absorber is a specific LHP configured with external fins, internal wicks and a top-positioned three-way tube (the vapor-liquid separation structure). This pipe enables water evaporation on its inner surface when receiving solar irradiation on the outer surface. To maintain the continuous operation of this process, the top three-way tube is a dedicated design, as shown schematically in **Fig. 2-1 (b)**, for the even distribution of water films across the inner-wall surface of the pipe, thus preventing the ‘dry-out’ potential of water across the wick surface. A piece of ‘人’-shaped copper tube with expanded edges is internally connected to a refined three-way copper fitting. When firmly compressing the bottom expander edge against the wick structure, the returned liquid is evenly distributed from the top of the evaporator across the wick surface owing to the equivalent capillary force within the wick structure. The three-way tube, meanwhile, can also deliver the vapor upward to the flat-plate exchanger from the inside through the vapor transportation line. This creates a clear separation between the liquid and vapor flows in the heat pipe.

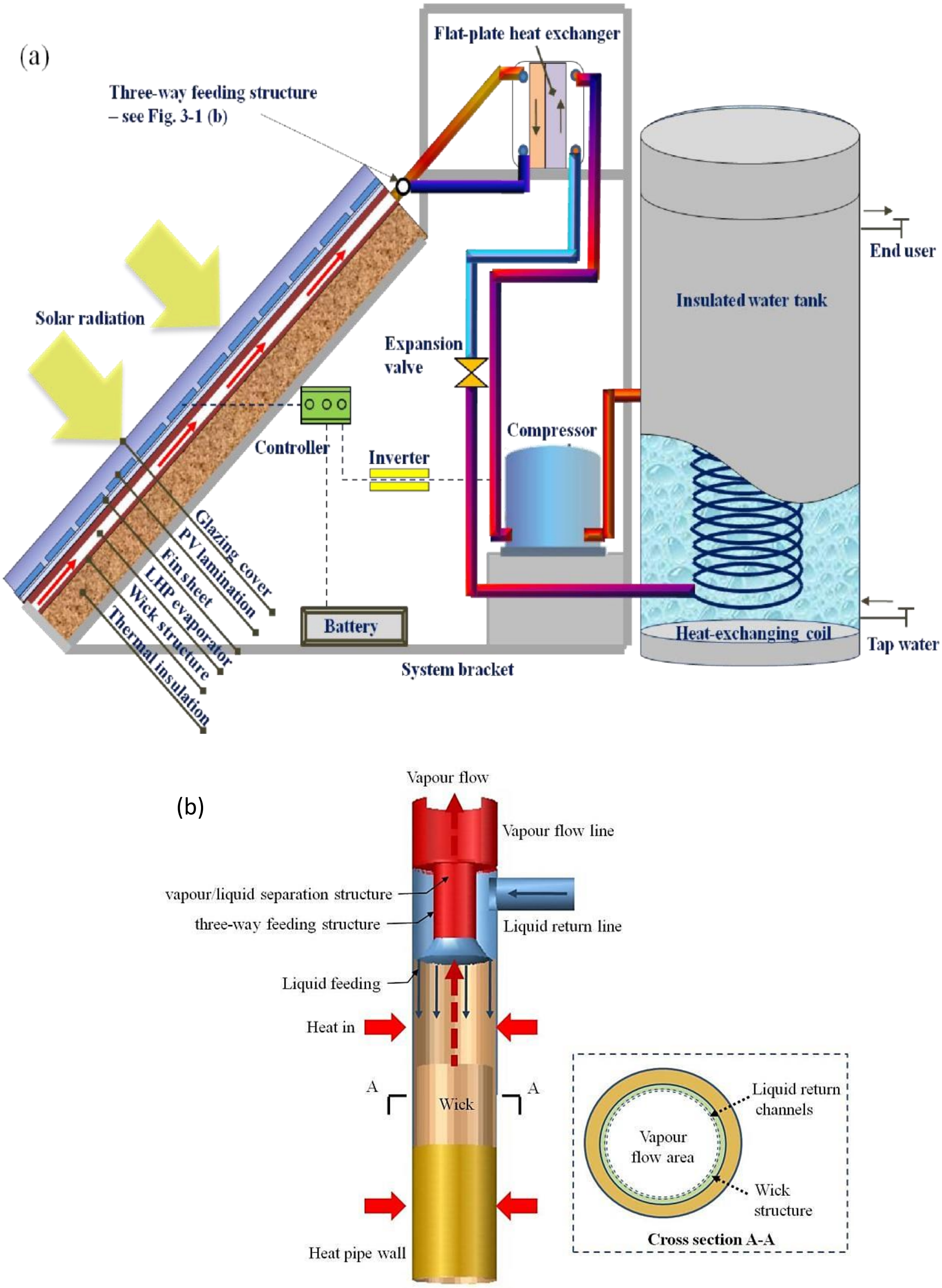

Fig. 2-1: *Schematics of (a) the heat pump-assisted PV/LHP solar water heating system and (b) concept design of the LHP three-way Vapor-liquid separation structure* [11]

In the PV/LHP module, the LHP device is fitted underneath the PV layer, as shown in **Fig. 2-2 (a)**. During normal operation, the heat is delivered to the flat-plate heat exchanger, then transferred to the refrigerant of heat pump, leading to condensation of the heat pipe working fluid. The condensed liquid returns to the LHP absorber via the liquid transportation line, completing the heat pipe fluid cycle. Moreover, an Al-alloy base sheet coated with anodic oxidation film was also used to replace the conventional TPT baseboard of PV cells during the module lamination process, besides of the enhanced EVA thermal conductivity. **Fig. 2-2 (b)** indicates the configuration of the Al-alloy-based PV layer. It consists of clean tempered glass on the top, a group of PV cells in the middle, a treated Al-alloy sheet at the back and two layers of Boron Nitide doped EVA sealant to connect all three components [11].

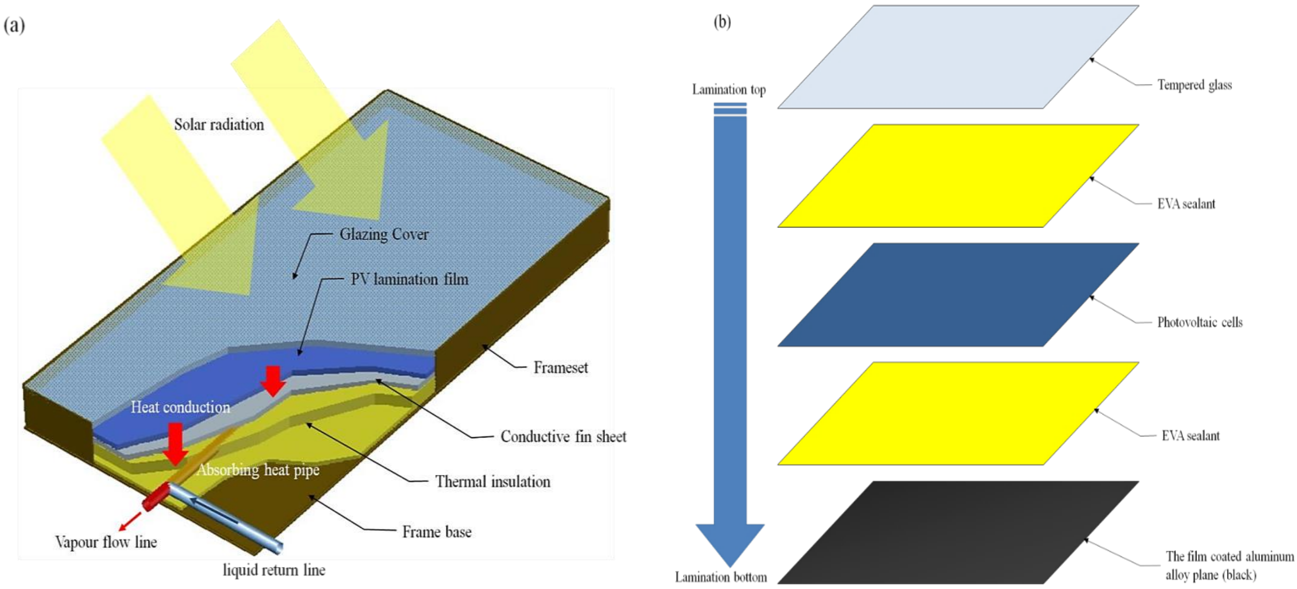

Fig. 2-2: *Concept design of (a) the PV/LHP collector and (b) configuration of the PV layer* [11]

In the heat pump cycle, the liquid refrigerant is vaporized in the heat exchanger, which, under the pressurization of the compressor, is converted into higher pressure, supersaturated vapor. Thus transfers heat energy into the tank water via the serpentine (condenser for the heat pump cycle), leading to a temperature increase in the tank water. The heat transfer process within the coil exchanger also leads to the condensation of the high pressure, supersaturated vapor, which, when passing through the expansion valve, is downgraded to a low-pressure liquid refrigerant. This refrigerant undergoes an evaporation process within the flat-plate heat exchanger (the evaporator for the heat pump cycle), thus completing the whole heat pump cycle.

A temperature-entropy (T-S) chart based on the thermodynamic cycle of the refrigerant within the heat pump cycle is displayed schematically in **Fig. 2-3**, where the isentropic efficiency is taken into account at the compressor for analysis, as additional power will be consumed in the practical operation.

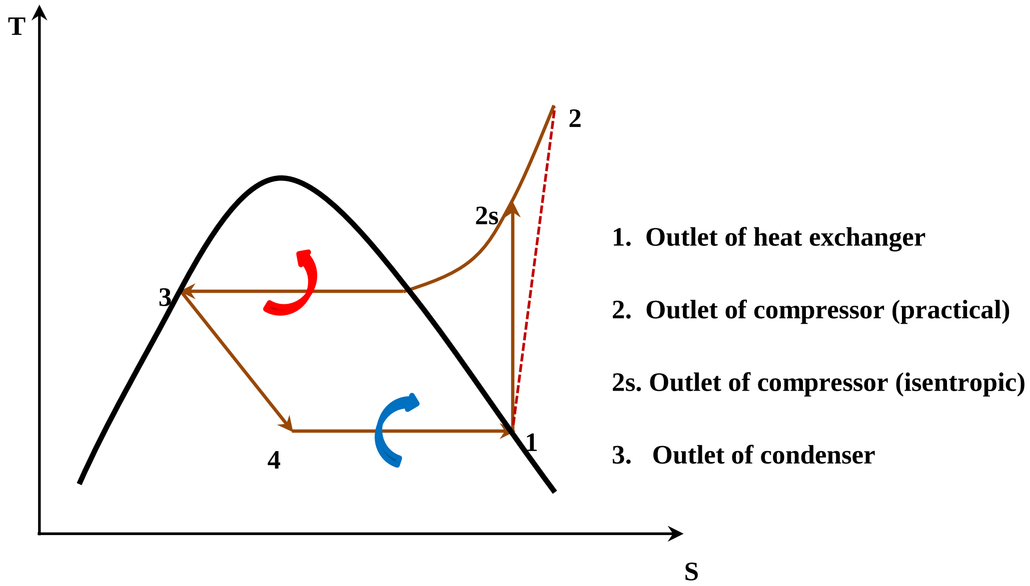

Fig. 2-3: *Heat pump thermodynamic cycle in a Temperature-Entropy chart*

The special features of the PV/LHP heat pump system lie in the following: (1) the temperature of the LHP working fluid can be controlled to a lower value through adjustment of the evaporation pressure of the refrigerant in the heat pump cycle; this will lead to reduced PV cell temperature, increased PV electrical and thermal efficiencies, and increased solar output per unit of absorbing surface; (2) the refrigerant temperature/pressure will be increased to the required level using a compressor to enable heat to be moved from the refrigerant to the hot water; (3) the power desired for compressor operation can be supplied by PV-generated electricity thus creating a low (zero) carbon heating operation.

II.3. Parameters of the New PV/LHP Heat Pump System

The variables used in subsequent theoretical analysis are summarized in **Table 2-1**.

Table 2-1: *Summary of different parameters for further characterization*

Parameter type		**Variables for characterization**
	Structure	(1) Glazing cover
		(2) LHP wick type
		(3) LHP numbers
Design parameters		
	Geometry	(1) LHP evaporator diameter
		(2) LHP evaporator length
		(3) LHP vapor column diameter in three-way fitting
		(4) LHP evaporator-to-condenser height difference
	Material	(1) PV baseboard
Operating parameters		(1) LHP operational temperature
		(2) LHP evaporator inclination angle (tilt angle)
		(3) LHP liquid filling mass
		(4) Heat pump evaporation temperature
		(5) PV mounting solution
External conditions		(1) Solar radiation
		(2) Air temperature
		(3) Air velocity
		(4) Operating time

II.4. Parametric Design of System Components

II.4.1. Glazing Cover

The glazing cover of the PV/LHP module is significant to the overall absorption of solar energy it also protects the PV/LHP module from external damage.

Table 2-2: *Parameters for the glazing cover* [11].

Glazing type	Emissivity	Transmittance	Thickness (m)	Conductivity (W/m-k)
Single	0.89	0.92	0.004	2.4

II.4.2. Al-alloy-based PV Layer

With absorbing area of 0.612 m^2. This layer consisted of 36 (4 × 9 array) PV cells, each with a size of 125 × 125 × 0.3 (mm × mm × mm), and covered nearly 90% of the baseboard surface.

Table 2-3: *Design Parameters of the Al-alloy-based PV panel* [11].

Parameters	**Nomenclature**	**Value**	**Unit**
Number of PV cells	N_{PV}	36 (4 × 9)	-
Packing ratio	β_{PV}	0.9	-
Nominal efficiency	$\eta_{PV,o}$	16.8	%
Thermal conductivity of Al-alloy	k_{Al}	144	W/m-K
Solar absorptance of Al-alloy	α_{Al}	5	%
Solar transmittance of Al-alloy	τ_{Al}	0.2	%
Thickness of Al-alloy	δ_{Al}	0.5	mm

II.4.3. LHP with Fin Sheet

The working fluid used in the Loop Heat Pipe is a solution of water and glycol (95%/5%). A 5mm thick aluminium Ω-type fin sheet wrapped the LHP evaporation section. The LHP wall is a copper material with a high thermal conductivity of 394 W/(m-K).

Table 2-4: *wick structure in the LHP evaporator* [11].

Parameters		**Nomenclature**	**Value**	**Unit**
Mesh screen	Wire diameter (layer I)	$D_{owi,ms}$	7.175×10^{-5}	m
	Layer thickness (layer I)	$\delta_{owi,ms}$	3.75×10^{-4}	m
	Mesh number (layer I)	$N_{owi,ms}$	6299	/m
	Wire diameter (layer II)	$D_{iwi,ms}$	12.23×10^{-5}	m
	Layer thickness (layer II)	$\delta_{iwi,ms}$	3.75×10^{-4}	m
	Mesh number (layer II)	$N_{iwi,ms}$	2362	/m
	Conductivity	$k_{s,ms}$	394	W/m-K

The liquid fill level is considered to be one-third to one-fourth of the evaporator length [51]. The height difference between the LHP condenser and absorber determines the capillary limit due to the gravity effort. The specifications of the loop components are listed in **Table 2-5**.

Table 2-5: *Design parameters of the LHP operation* [11].

Parameters	Nomenclature	Value	Unit
External diameter of evaporator	$D_{hp,o}$	0.022	m
Internal diameter of evaporator	$D_{hp,in}$	0.0196	m
Internal diameter of vapor column	D_{vt}	0.018	m
Operating temperature range	T_v	20-60	°C
Vacuum pressure in heat pipe	P_{hp}	1.3×10^{-4}	Pa
Evaporator length	$L_{hp,e}$	1.2	m
Evaporator inclination angle	φ_e	0-90	deg.
Evaporator-to-condenser height difference	$H_{hx,hp}$	1.0	m
Liquid filling mass	m_{fl}	0.001-0.045	kg
Transportation line outer diameter	$D_{ltl,o}$ / $D_{vtl,o}$	0.022	m
Transportation line inner diameter	$D_{ltl,in}$ / $D_{vtl,in}$	0.0196	m
Transportation line length	L_{ltl} / L_{vtl}	1.0/0.9	m
Fin sheet (length/width)	L_{fin}/W_{fin}	1.2/0.55	m

Table 2-6 presents the properties of water at different operating temperature levels [52-53]. The thermodynamic properties of the water/glycol mixture can be considered to be approximately the same as water when the glycol only accounts for less than 5% of the total liquid volume.

Table 2-6: *Thermodynamic properties of water with operating temperatures*

T_v °C	h_{fg} kJ/kg	P_v Pa	ρ_v kg/m^3 (e-02)	ρ_l kg/m^3	k_l W/k-m	μ_v kg/m-s (e-06)	μ_l kg/m-s (e-04)	σ N/m (e-02)
20	2454	2337	1.73	998	0.600	8.84	10.00	7.28
25	2442	3172	2.38	997	0.613	9.03	8.70	7.20
30	2430	4242	3.04	996	0.621	9.22	8.03	7.12
35	2418	5622	4.08	994	0.627	9.42	7.16	7.04
40	2407	7375	5.12	992	0.634	9.62	6.45	6.96
45	2395	9582	6.71	990	0.64	9.82	5.98	6.88
50	2393	12335	8.30	988	0.645	10.00	5.53	6.79
55	2371	15740	10.70	986	0.650	10.20	5.09	6.71
60	2358	19920	13.00	983	0.654	10.40	4.71	6.62

II.4.4. Flat-plate Heat Exchanger

It comprises a series of thin and corrugated thermal plates commonly made of stainless steel, which are compressed together into a frame to form an arrangement of parallel flow channels with alternating hot and cold fluids. In comparison to shell-and-tube heat exchangers, plate-heat exchangers require a lower temperature and smaller size for the equivalent heat exchanged [54].

Table 2-7: *Design parameters of the flat-plate heat exchanger* [11].

Parameters	**Nomenclature**	**Value**	**Unit**
Heat exchanger plate thickness	δ_{hx}	0.00235	m
Heat exchanger plate height	H_{hx}	0.206	m
Heat exchanger plate cluster width	W_{hx}	0.076	m
Heat exchanger plate cluster length	L_{hx}	0.055	m
Heat exchanger number of plates	N_{hx}	20	-
Heat exchanger operating temperature range	T_{hx}	-160-225	ºC
Heat exchanger operating pressure range	P_{hx}	0-3.24	MPa

II.4.5. Heat Pump

The environmentally friendly R134a was considered as the working fluid. The evaporation and condensation temperatures are set at 0 – 25 ºC and 55 ºC, respectively. A water tank with embedded copper heat-exchanging coil is connected to the heat pump, acting as its condenser and hot water storage. The thermodynamic properties for each point (1, 2s, 3 and 4 in **Fig. 2-3**) are displayed in **Table 2-8** through "Solkane v8", a special program developed to calculate properties of all refrigerants.

Table 2-8: *Sample thermodynamic properties of the R134a refrigerant in the heat pump*

Point	**Phase**	**Pressure (MPa)**	**Temperature (ºC)**	**Enthalpy(H) (kJ/kg)**	**Entropy(S) (kJ/kg·K)**
1	Vapor	0.5717	20	409.748	1.71804
2s	Vapor	1.4915	58.34	429.449	1.71804
3	Liquid	1.4915	55	279.469	1.26106
4 (x[1]=0.2853)	Liquid/Vapor	0.5717	20	279.469	1.27363

[1] Note: *x means the saturation of refrigerant*

II.4.6. Insulation Material

Table 2-9: *Thermal resistance of typical insulating materials*

Insulating materials	Thermal resistance (K-m²/W)
Polyurethane foam	0.986-1.356

II.5. Chapter Conclusion

This chapter has described the system concept and its working principles from the aspects of the PV/LHP module, the LHP and the heat pump. The different features of the PV/LHP heat pump system lay in the following: (1) the temperature of the LHP working fluid can be controlled to a lower level through tuning of the refrigerant evaporation pressure in the heat pump cycle; (2) the refrigerant temperature/pressure would be raised to the required level using a compressor; (3) the power desired for compressor operation could be provided by the PV-generated electricity.

The chapter also presented the parametric design of the different system components, including the glazing cover, PV layer, LHP, fin sheet, flat-plate heat exchanger, heat pump, and insulation material.

Chapter III:

Theoretical Analysis

III. Theoretical Analysis and Development of The Computer Simulation Models

III.1. Chapter Introduction

Based on the established conceptual design, this chapter reports the theoretical analysis and development of the associated computer simulation models. The theories are coupled with the energy balance equations within different parts of the system, including transient solar transmittance, heat transfer, fluid flow and photovoltaic generation. The main works achieved are described in this chapter as follows:

(1)Two theoretical models were built, respectively, for the LHP heat transfer limits and the dynamic performance.

(2)The iterative method (IM), backward differentiation formula (BDF or Gear's method) and finite element method (FEM) were applied to solve the mathematical models by means of computer.

(3)A group of computer-based simulation models were subsequently developed to simulate the performance of the LHP device and the integrated PV/LHP heat pump system

III.2. Analytical Model for the LHP Heat Transfer Limit

III.2.1. Modelling Objective for the LHP Heat Transfer Limit

Analysis of the LHP heat transfer limit is required prior to the investigation of the integrated system. Once the maximum LHP heat transfer value was determined, the size and capacity of other system components could be determined. Development of an analytical model for the LHP device enabled (a) maximum heat transfer capacity of the LHP device at the given geometric setting and operational condition; (b) determination of the LHP operational performance against different variables.

III.2.2. Thermal Fluid Theory and the Associated Mathematical Equations of the LHP Heat Transfer Model

A schematic showing the LHP operation is displayed in **Fig. 3-1**. Ideally, the liquid flowing across the wick can be instantly evaporated without or with little reservation at the bottom of the LHP evaporator during operation, which will help maximize the heat transport capacity of the LHP. This configuration can create an even distribution of the liquid across the evaporator wick surface, which will result in enhanced heat transfer capacity over conventional LHP systems.

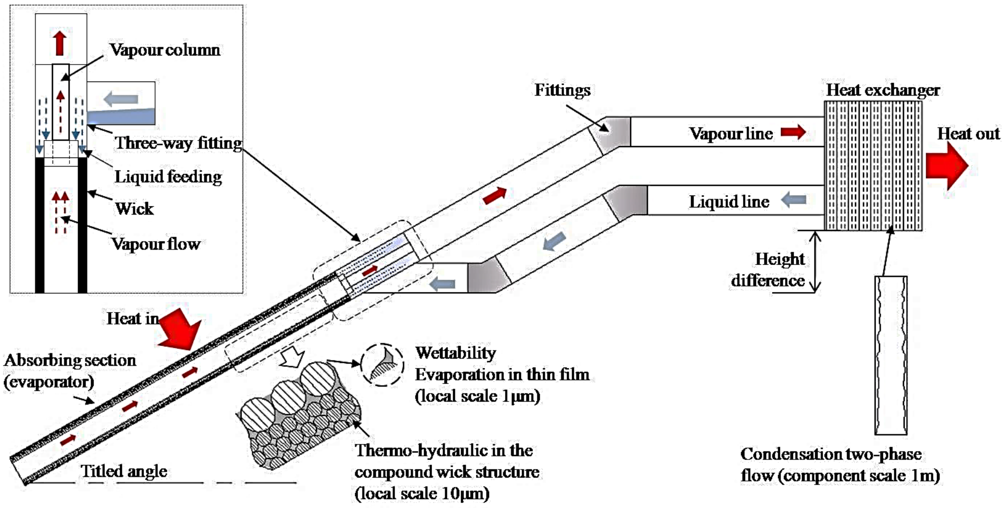

Fig. 3-1: *Schematic of the thermal and hydrodynamic couplings in the LHP* [11]

In this section, six limits will be discussed in determining the LHP heat transport capacity, i.e., the viscous, sonic, entrainment, capillary, boiling and liquid filling mass limits. The minimum values of these limitations are the actual restraint on the system heat transfer. The magnitudes of these limits are directly related to the thermal properties of the working fluids, wick structures, heat pipe dimensions, and operating conditions, each expression of these limits will be applied on all LHP components by replacing the corresponding parameters and characteristics of considered LHP component. The minimum value among these items will be the ultimate limit.

(1) Viscous Limit, Q_{VL}

At low-temperature operation, the viscous forces dominate the performance of vapor flow. Bussel et al. [48] initially developed an equation for the viscous limit

$$Q_{VL,e} = \frac{\pi D_{v,e}^4 h_{fg} \rho_v P_v}{256 \mu_v L_e} \qquad [3-1]$$

where, $Q_{VL,e}$ is the viscous limit at the absorbing section (W); $D_{v,e}$ and L_e are the diameter (m) and length (m)of vapor space in the absorbing section; h_{fg}, ρ_v, μ_v and P_v are the thermodynamic properties of the vapor at certain operating temperature respectively, which are the latent heat of vaporization (J/kg), density (kg/m^3), dynamic vapor viscosity (kg/m-s), and corresponding saturated vapor pressure (Pa).

$$Q_{VL} = min\left(Q_{VL,e}\, , Q_{VL,vt}\, , Q_{VL,vtl}\, , Q_{VL,hx}\right) \qquad [3-2]$$

(2) Sonic Limit, Q_{SL}

At higher temperature operation, the Mach number of the vapor will increase significantly. Particularly when the vapor velocity is close to the sonic or supersonic level, the compression state of the vapor should be taken into consideration to evaluate its heat transfer capacity. A heat pipe may be choked by high-speed vapor flow, which would limit the total heat transfer capacity in the pipe. This limit for the evaporator is given by [56]

$$Q_{SL,e} = \left(\frac{\pi D_{v,e}^{2} \rho_v h_{fg}}{4}\right) \left[\frac{\gamma_v R_v T_v}{2(\gamma_v + 1)}\right]^{0.5} \qquad [3-3]$$

where, $Q_{SL,e}$ is the sonic limit at the absorbing section (W); γ_v is the vapor specific heat ratio whose magnitude is 4/3 for polyatomic working liquid (water); T_v is the average vapor temperature (K) in the absorbing section; R_v, is the vapor constant (kJ/kg-K), given by:

$$R_v = \frac{R_0}{m} \qquad [3-4]$$

where, R_0 is the universal gas constant ($R_0 = 8.314$kJ/kmol·k); m is the molecular weight of the vapor (m = 18 for water).

$$Q_{SL} = min\left(Q_{SL,e}\, , Q_{SL,vt}\, , Q_{SL,vtl}\, , Q_{SL,hx}\right) \qquad [3-5]$$

(3) Entrainment Limit, Q_{EL}

The opposite flow directions of liquid and vapor may result in shear force at the liquid-vapor interface. When the vapor velocity is sufficiently high, the liquid will be torn from the wick surface and entrained into the vapor [56]. Entrainment can lead to a sudden substantial increase in fluid circulation and, consequently, the immediate drying out of the wick at the evaporator. The expression of this limit at the evaporator is given as [56]

$$Q_{EL,e} = \left(\frac{\pi D_{v,e}^{2} h_{fg}}{4}\right) \left[\frac{\sigma \rho_v}{2 r_{h,s}}\right]^{0.5} \qquad [3-6]$$

where, σ is the surface tension coefficient of water (N/m); $r_{h,s}$ is the hydraulic radius of wick surface pore (m), for a ***screen mesh*** wick which is given by

$$r_{h,s} = \left(\frac{1}{N_{iwi,ms}} - D_{iwi,ms}\right)/2 \qquad [3-7]$$

where, $N_{wi,in}$ and $D_{w,ins}$ are mesh number (1/m) and wire diameter of the inner screen layer (m).

$$Q_{EL} = min\left(Q_{EL,e}\,,\,Q_{EL,hx}\right) \qquad [3-8]$$

(4) Capillary Limit, Q_{CL}

The capillary limit represents the ability of heat pipe wicks to carry over the maximum liquid flow. A heat pipe has a higher heat transport capacity with a larger volume of liquid pumped by wicks [57]. During heat pipe operation, the maximum capillary pumping head ($\Delta P_{c,max}$, Pa) must be greater than or at least equal to the total pressure drops along the heat pipe. The pressure drops consist of three aspects [56]: the viscous and inertial drop in the vapor (ΔP_v, Pa); the viscous drop in the liquid (ΔP_l, Pa); and the gravitational head (ΔP_G, Pa), which contains radial and axial hydrostatic pressure drops (ΔP_{rG} and ΔP_{aG}). For this particular operation, where the heat pipe fluid is mainly driven by gravity, the overall gravitational head is positive. The pressure relationship is

$$\Delta P_{c,max} + \Delta P_G \geq \Delta P_v + \Delta P_l \qquad [3-9]$$

a. Maximum Capillary Head ($\Delta P_{c,max}$)

The capillary pressure power across a curved liquid-vapor interface achieves the maximum value when the contact angle in the evaporator (θ_e) equals zero and in the condenser (θ_c) is π/2 (see **Fig. 3-2**). The maximum capillary pressure for such LHP operations is given by [49]

$$Q_{EL,e} = \frac{2\sigma cos(\theta_e)}{r_e} \qquad [3-10]$$

where, r_e is the effective capillary radius (m) which has the different expressions with wick structures, for a ***compound mesh screen*** wick

$$r_e = \frac{1}{2N_{owi,ms}} \qquad [3-11]$$

where, $N_{wi,o}$ is the mesh number of the outer screen layer (1/m).

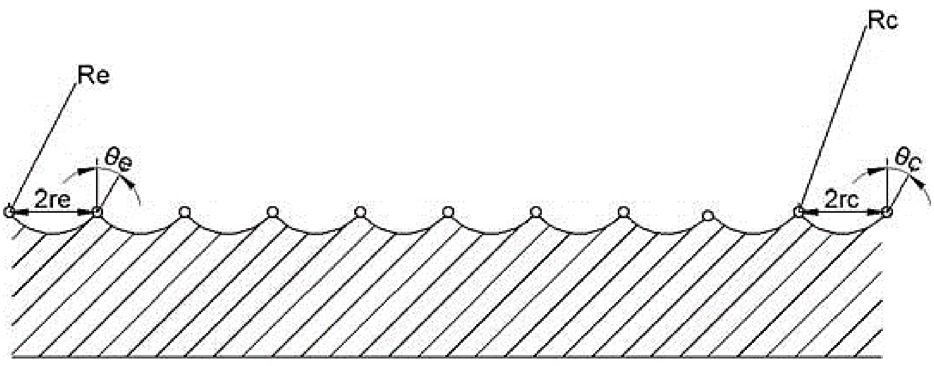

Fig. 3-2: *Wick and pore parameters in the evaporator and condenser*

Zhao [57] recommended that the contact angle (θ) should be about $\pi/3$ for any heat pipe application. Imura et al. [58] suggested that the theoretical capillary force should be multiplied by a correction ratio of 2/3 for a mesh-screen wicked heat pipe design. These correction factors are necessary for the determination of the actual capillary power of this LHP during practical design.

b. Gravity Pressure Head (ΔP_G)

If a heat pipe works at a gravitational field and the circumferential communication of liquid in the wick is possible, the radial hydrostatic pressure drop has to be considered, and is the effort of liquid rising in a direction perpendicular to the heat pipe axis against the force of gravity, expressed by

$$\Delta P_{rG} = -\rho_l g D_{v,e} cos\phi \qquad [3-12]$$

where, ρ_l *is* the liquid density (kg/m^3); Φ is the collector title angle (rad). The positive axial hydrostatic pressure head of the liquid column is generated by the overall height difference between the heat pipe condenser and the bottom of the evaporator. This pressure difference is

$$\Delta P_{aG} = \rho_l g \left(H_{hx}/2 + H_{hx-hp} + L_e sin\phi \right) \qquad [3-13]$$

where, H_{hx} is the height of the heat exchanger plate (m); $H_{hx\text{-}hp}$ is the height difference between the heat exchanger and the top of absorbing heat pipes (m).

Thus, the overall gravity head is

$$\Delta P_G = \Delta P_{aG} - \Delta P_{rG} \qquad [3-14]$$

c. Vapor Pressure Drop (ΔP_v)

A vapor pressure drop (ΔP_v) occurs in four LHP parts, including the evaporator ($\Delta P_{v,e}$), the vapor column of the three-way fitting ($\Delta P_{v,vt}$), the vapor transportation line ($\Delta P_{v,vtl}$), and the condenser section ($\Delta P_{v,hx}$)

$$\Delta P_{v} = \Delta P_{v,e} + \Delta P_{v,vt} + \Delta P_{v,vtl} + \Delta P_{v,hx} \qquad [3-15]$$

i. Vapor Pressure Drop in the Evaporator ($\Delta P_{v,e}$), the Vapor Column of the Three-way Fitting ($\Delta P_{v,vt}$), and the Vapor Transportation Line ($\Delta P_{v,vtl}$)

The vapor pressure gradient at the evaporator can be written as [56]

$$\Delta P_{v,e} = F_{v,e} L_e Q_{CL} \qquad [3-16]$$

where, Q_{CL} is the capillary limit (W); $F_{v,e}$ is the vapor frictional coefficient in the absorbing section, given by

$$F_{v,e} = \frac{8C_{v,e}\left(f_{v,e}Re_{v,e}\right)\mu_v}{\pi D_{v,e}^4 \rho_v h_{fg}} \qquad [3-17]$$

where, $C_{v,e}$ and $f_{v,e}$ are the characteristic parameter and the friction factor in the absorbing section, which can be determined once the local axial Reynolds number and Mach number are defined. These expressions are given below

$$Re_{v,e} = \frac{4Q_{CL}}{\pi D_{v,e}\mu_v h_{fg}} \qquad [3-18]$$

$$M_{v,e} = \frac{4Q_{CL}}{\pi D_{v,e}^2 \rho_v h_{fg}(R_v T_v \gamma_v)^{0.5}} \qquad [3-19]$$

Kraus and Bar-Cohen [59] gave the full expression of $C_{v,e}$ and $f_{v,e}$ with different conditions

$Re_{v,e} \le 2300,\ M_{v,e} \le 0.2$:

$$\left(f_{v,e}Re_{v,e}\right) = 16,\ C_{v,e} = 1.00 \qquad [3-20]$$

$Re_{v,e} \le 2300,\ M_{v,e} > 0.2$:

$$\left(f_{v,e}Re_{v,e}\right) = 16,\ C_{v,e} = \left(1 + \left(\frac{\gamma_v - 1}{2}\right) M_{v,e}^2\right)^{-0.5} \qquad [4-21]$$

$Re_{v,e} > 2300, M_{v,e} \leq 0.2$:

$$\left(f_{v,e}Re_{v,e}\right) = 0.038, C_{v,e} = Re_{v,e}^{0.75} \qquad [3-22]$$

$Re_{v,e} > 2300, M_{v,e} > 0.2$:

$$\left(f_{v,e}Re_{v,e}\right) = 0.038, C_{v,e} = \left(1 + \left(\frac{\gamma_v - 1}{2}\right) M_{v,e}^{2}\right)^{-0.75} Re_{v,e}^{0.75} \qquad [3-23]$$

The vapor pressure gradient at the vapor column in the three-way fitting ($\Delta P_{v,vt}$) and vapor transportation line ($\Delta P_{v,vtl}$) can be similarly carried out using the equations from [3-12] to [3-19] by substituting the evaporator's parameters (i.e., diameter and length of the vapor flow) with the respective characteristic parameters in each vapor core space of the LHP.

ii. Vapor Pressure Drop in the Condenser Section ($\Delta P_{v,hx}$)

As the vapor channels in the heat exchanger have the same structure/geometry and are connected in parallel with the same amount of vapor passing across, the vapor pressure drop in one plate could represent a pressure loss in the whole condenser section. For a single plate, the vapor pressure drop is [60]

$$\Delta P_{v,hx} = F_{v,hx}\left(\frac{H_{hx}}{2}\right)\left[\frac{Q_{CL}}{(N_{hx}/2) - 1}\right] \qquad [3-24]$$

where, N_{hx} is the number of heat exchanger plates; $F_{v,hx}$ is the vapor frictional coefficient in the heat exchanger, which can be similarly determined through equations [3-13] to [3-19] by substituting the evaporator's hydraulic diameter with the characteristic diameter of the vapor space in the heat exchanger.

d. Liquid Pressure Drop (ΔP_l)

A liquid pressure drop (ΔP_l) also occurs in four parts, i.e., the condenser section ($\Delta P_{l,hx}$), the liquid transportation line ($\Delta P_{l,ltl}$), the liquid feeding inlet ($\Delta P_{l,lt}$) of the three-way fitting, and the evaporating section ($\Delta P_{l,e}$). The overall liquid pressure drop is, therefore, defined by

$$\Delta P_l = \Delta P_{l,hx} + \Delta P_{l,ltl} + \Delta P_{l,lt} + \Delta P_{l,e} \qquad [3-25]$$

i. Liquid Pressure Drop in the Condenser Section ($\Delta P_{l,hx}$)

The liquid pressure drop in each heat exchanger plate channel can represent a total liquid pressure drop in the condenser. For a single-plate channel, the liquid pressure drop can be described using Darcy's Law [56]

$$\Delta P_{l,hx} = F_{l,hx}\left(\frac{H_{hx}}{2}\right)\left[\frac{Q_{CL}}{(N_{hx}/2)-1}\right] \qquad [3-26]$$

where, $F_{l,hx}$ is the liquid frictional coefficient in the heat exchanger, defined as

$$F_{l,hx} = \frac{4\mu_l}{\pi\left(D_{hx}^2 - D_{lf}^2\right)\rho_l h_{fg}} \qquad [3-27]$$

where, D_{hx} and D_{lf} are respectively the hydraulic diameters of plate (m) and liquid film in the heat exchanger (m); μ_l is the dynamic viscosity of the working liquid (kg/m-s).

ii. Liquid Pressure Drop in the Liquid Line ($\Delta P_{l,ltl}$) and the Three-way Fitting ($\Delta P_{l,lt}$)

The liquid pressure drop in the liquid transportation line is [56]

$$\Delta P_{l,tl} = F_{l,ltl} L_{ltl} Q_{CL} \qquad [3-28]$$

where, L_{ltl} is the length of the liquid transportation line (m); $F_{l,tl}$ is the liquid frictional coefficient in the liquid transportation line, defined as

$$F_{l,ltl} = \frac{4\mu_l}{\pi D_{l,ltl}^2 \rho_l h_{fg}} \qquad [3-29]$$

where, $D_{l,ltl}$ is the diameter of liquid core in the liquid transportation line (m).

The liquid pressure gradient in the three-way feeding structure ($\Delta P_{l,lt}$) can be similarly carried out through equations [3-24] and [3-25] by substituting the length and diameter of the liquid line with the respective characteristic parameters of the three-way fitting.

iii. Liquid Pressure Drop in the Evaporator ($\Delta P_{l,e}$)

The liquid pressure drop in the evaporator is written as [56]

$$\Delta P_{l,e} = F_{l,e} L_e Q_{CL} \qquad [3-30]$$

where, $F_{l,e}$ is the liquid frictional coefficient in absorbing pipe, given as

$$F_{l,e} = \frac{\mu_l}{K_p A_w \rho_l h_{fg}} \qquad [3-31]$$

where, A_w is the cross sectional area of liquid flow in the wick (m^2); K_p is the wick permeability (m^2), which varies with different types of wick structures:

For a ***compound mesh screen*** wick structure, the cross area of the liquid flow and its permeability can be determined by the inner screen layer, given by [57]

$$A_w = \pi\left(D_{iwi,in}^2 - D_{v,e}^2\right)/4 \qquad [3-32]$$

where, $D_{iwi,in}$ is the diameter of inner screen layer in the absorbing pipe (m).

$$K_p = \frac{D_{iwi,ms}^2 \varepsilon_{iwi,ms}^3}{122\left(1-\varepsilon_{iwi,ms}\right)^2} \qquad [3-33]$$

where, $\varepsilon_{iwi,ms}$ is the porosity of inner mesh screen layer, written as

$$\varepsilon_{iwi,ms} = 1 - \frac{1.05\pi N_{iwi,ms} D_{iwi,ms}}{4} \qquad [3-34]$$

Combining the above equations yields the final expression of the capillary limit

$$Q_{CL} \le \frac{\Delta P_{c,max} + \Delta P_G}{\left(F_{v,e}L_e + F_{v,vt}L_{vt} + F_{v,ltl}L_{ltl} + \frac{F_{v,hx}H_{hx}}{N_{hx}-2}\right) + \left(F_{l,e}L_e + F_{l,ltl}L_{ltl} + F_{l,tl}L_{lt} + \frac{F_{l,hx}H_{hx}}{N_{hx}-2}\right)} \qquad [3-35]$$

(5) Boiling Limit, Q_{BL}

The boiling limit represents the maximum radial heat density at the evaporator and occurs at an extremely high heat pipe operational temperature, which causes burning out of the liquid at certain areas of the wicks or heat pipe wall. Similarly, a limited heat flux will exist in the condenser (heat exchanger) of the LHP. For the evaporator, the analytical expression is [56]

$$Q_{BL,e} = \frac{2\pi L_e k_{wi} T_v}{h_{fg}\rho_v ln\left(D_{hp,in}/D_{v,e}\right)}\left(\frac{2\sigma}{r_b} - P_{c,max}\right) \qquad [3-36]$$

where, r_b is the radius of the bubbles, which could be assumed at 2.54×10^{-7}m for the general estimation of a normal heat pipe performance; $P_{c,max}$ is the maximum capillary power (Pa), which can be ignored by comparing with the value of $2\sigma/r_b$; k_{wi} is the effective thermal conductivity of the liquid-saturated wick (W/m-K), for the outer ***mesh screen*** layer in cylindrical geometry, which is given by

$$k_{wi} = k_l \frac{(k_l + k_{s,ms}) - (1 - \varepsilon_{owi,ms})(k_l - k_{s,ms})}{(k_l + k_{s,ms}) + (1 - \varepsilon_{owi,ms})(k_l - k_{s,ms})} \qquad [3-37]$$

where, k_l and $k_{s,ms}$ are the thermal conductivities of liquid and outer screen layer (W/m-K). The effective thermal conductivity of the inner screen layer can be similarly obtained from above equation, thus the overall wick effective conductivity is simply expressed as

$$k_{s,ms} = \frac{k_{owi,ms} + k_{iwi,ms}}{2} \qquad [3-38]$$

$$Q_{BL} = min(Q_{BL,e}\,, Q_{BL,hx}) \qquad [3-39]$$

(6) Liquid Filling Mass Limit, Q_{FL}

The liquid filling mass limit is the minimum liquid level required to be filled into the loops, which affects the heat transportation capacity using liquid gravity force. This limit reflects the minimum amount of liquid that is fully circulated in the heat pipe loop with the assistance of gravity at a certain height. The liquid filling mass limit for the evaporator is [60]

$$Q_{FL,e} = \left(\frac{m_f}{xL_e}\right)^3 \frac{k_l g h_{fg}}{3\pi^2 \mu_l \rho_l D_{hp,in}^2} \qquad [3-40]$$

where, m_f is the filled liquid mass (kg); x is the parameter relating to the filled liquid mass, which is assumed at 0.8 for pipes with wick structure and 1.0 for those sections without wick.

III.2.3. Algorithm for the LHP Heat Transfer Model Development and Operation

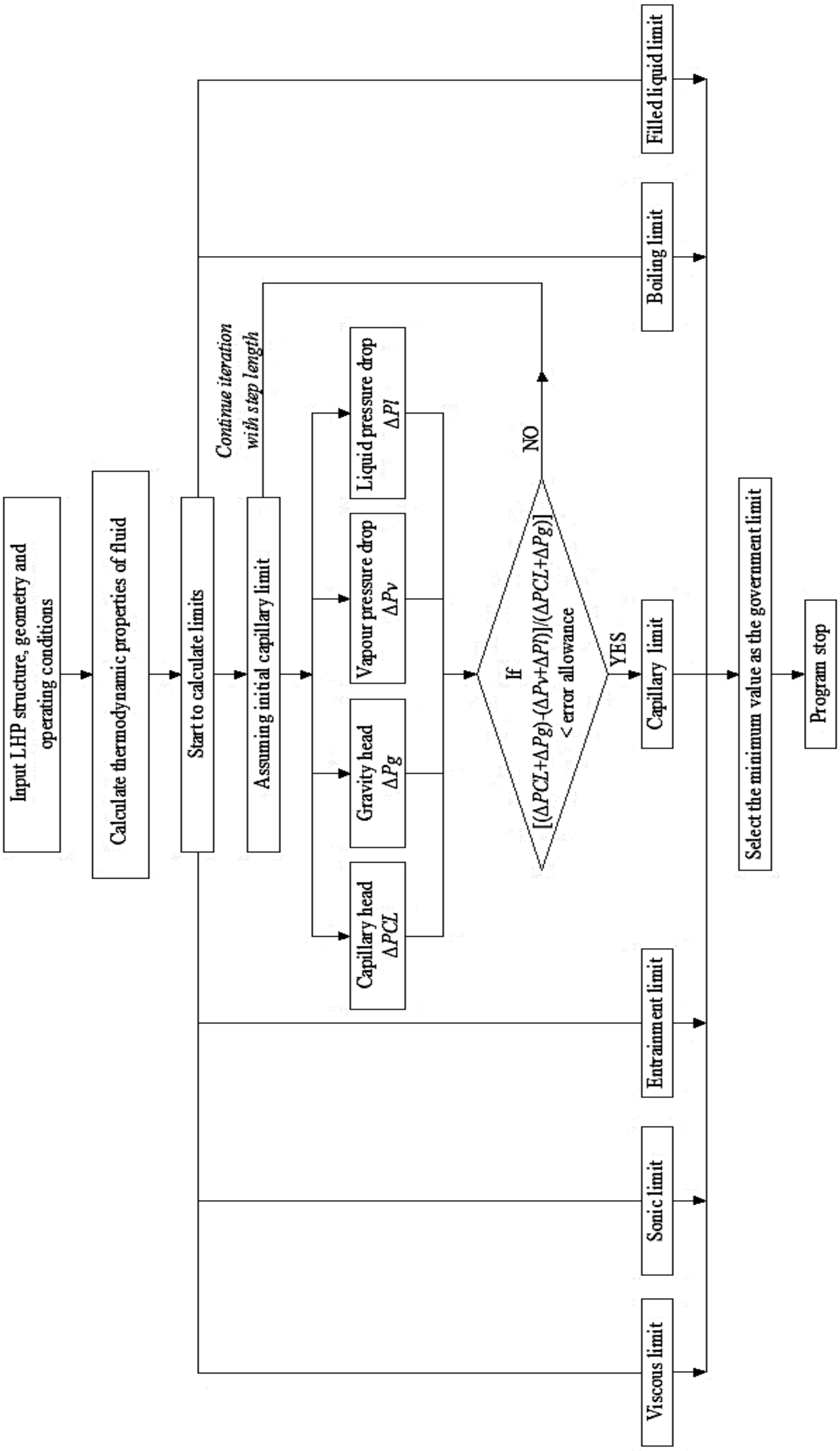

Fig. 3-3: *Flow chart for calculating the LHP heat transfer limits*

III.2.4. Result Discussion of LHP Heat Transfer Limit

The LHP's heat transfer capacity is a factor that depends upon its several operational and geometric parameters, i.e., working temperature, wick type, evaporator diameter/length, evaporator inclination angle, vapor column diameter in the three-way fitting, liquid filling level, and evaporator elevation above the condenser. The impacts of these parameters on LHP heat transfer capacity are presented in the following sections and the results are then discussed.

(1) Impact of Operational Temperature

Each vapor pressure figure within the LHP will be coupled with a corresponding saturated vapor temperature, termed as the operational temperature. Water vapor pressure in the LHP is considered as a function of temperature and can be determined with Clausius–Clapeyron relation [61]

$$P = 133.32exp\left(20.386 - \frac{5132}{T + 273.13}\right) \qquad [3-41]$$

where, T and P are the corresponding temperature (K) and vapor pressure (Pa) of water at certain thermodynamic status.

The relation between the heat pipe operational temperature and the heat transfer limits was simulated and the results are presented in **Fig. 3-4**. The capillary limit was found to be the governing limit.

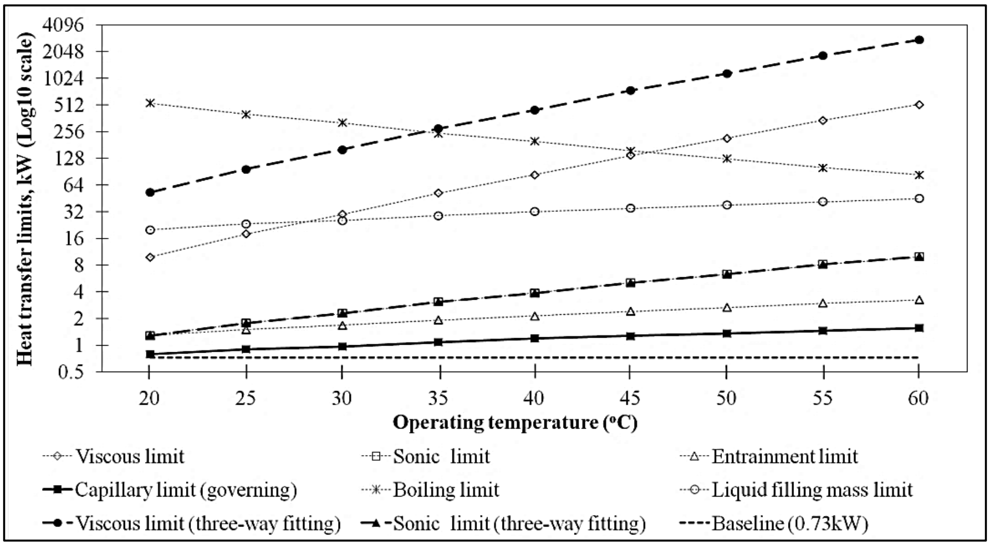

Fig. 3-4: *Impact of operational temperature on the heat transfer performance of the LHP* [62]

(2) Impact of Wick Structure

Correlation between different limits and mesh-screen structure is presented in **Table 3-1**.

Table 3-1: *Impact of wick structure on the heat transfer performance of the LHP* [62]

Wick type	Q_{VL}	Q_{SL}	Q_{EL}	Q_{CL}	Q_{BL}	Q_{FL}	Q_{L}
Screen mesh (kW)	17.93	1.77	1.50	**0.90**	401.29	23.26	**0.90**

(3) Impact of Evaporator Diameter

While the other loop operating and design parameters remained the same, the correlation between the evaporator diameter and the LHP heat transfer limit is presented in **Fig. 3-5**.

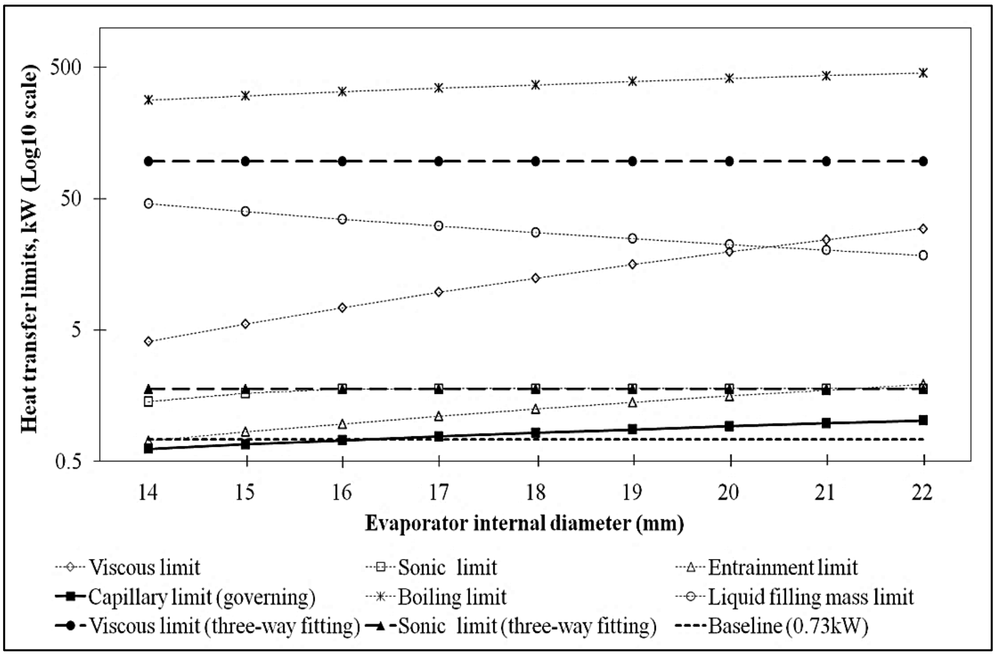

Fig. 3-5: *Impact of evaporator diameter on the heat transfer performance of the LHP* [62]

The capillary limit was found to be the governing limit for this operation.

(4) Impact of Evaporator Length

The correlation between the evaporator length and the LHP heat transfer limit is given in **Fig. 3-6**.

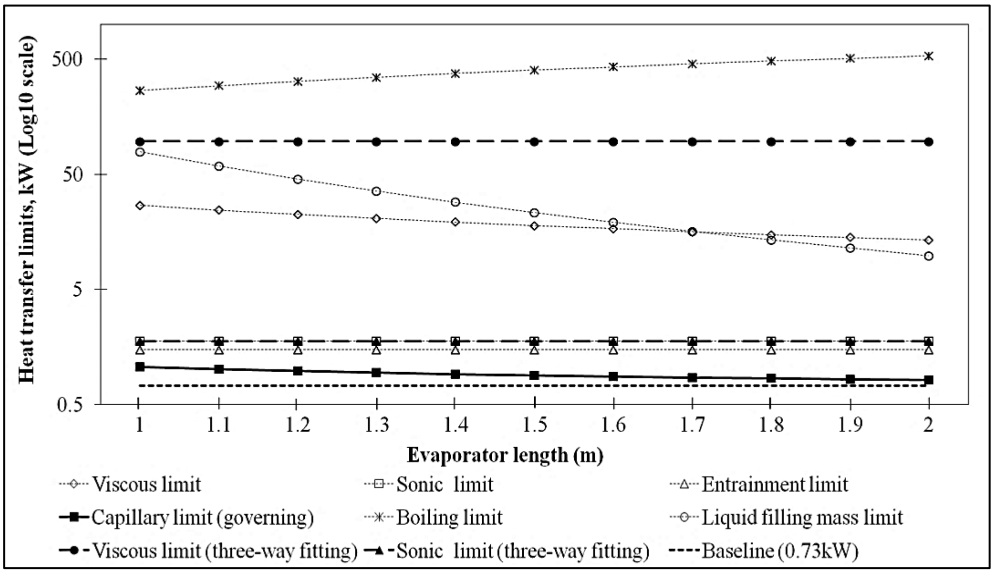

Fig. 3-6: *Impact of evaporator length on the heat transfer performance of the LHP* [62]

The capillary limit was also found to be the critical limit.

(5) Impact of Evaporator Inclination Angle

The correlation between the evaporator inclination angle and the LHP heat transfer limit is illustrated in **Fig. 3-7**.

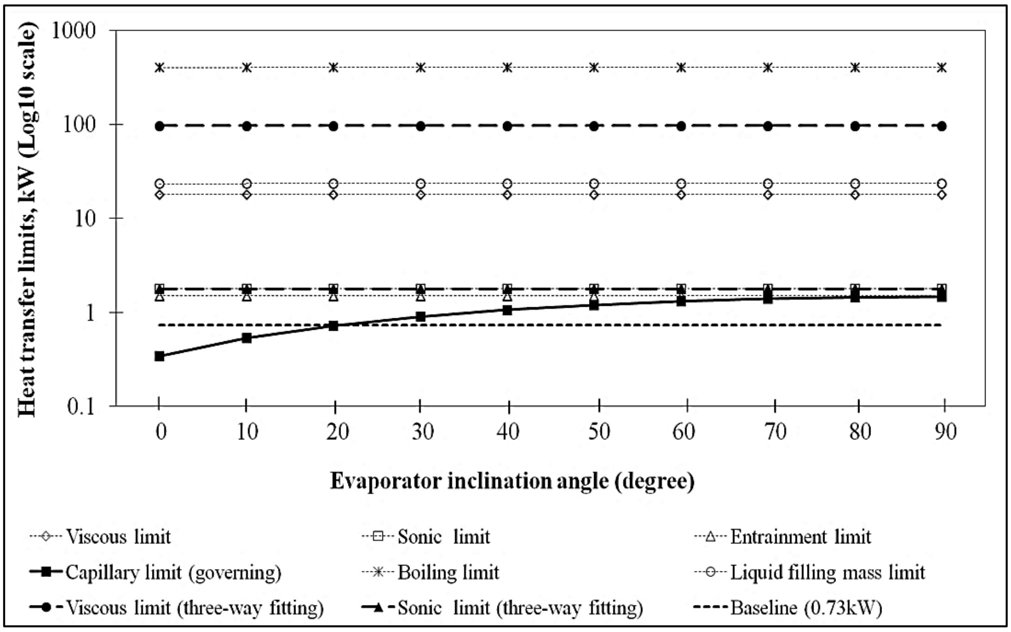

Fig. 3-7: *Impact of evaporator inclination angle on the heat transfer performance of the LHP* [62]

The capillary limit was observed as the primary limit in this case, which increased with the evaporator inclination angle, while the other five limits remained constant.

(6) Impact of Vapor Column Diameter

The correlation between the vapor column diameter in the three-way fitting and the LHP heat transfer limit is shown in **Fig. 3-8**.

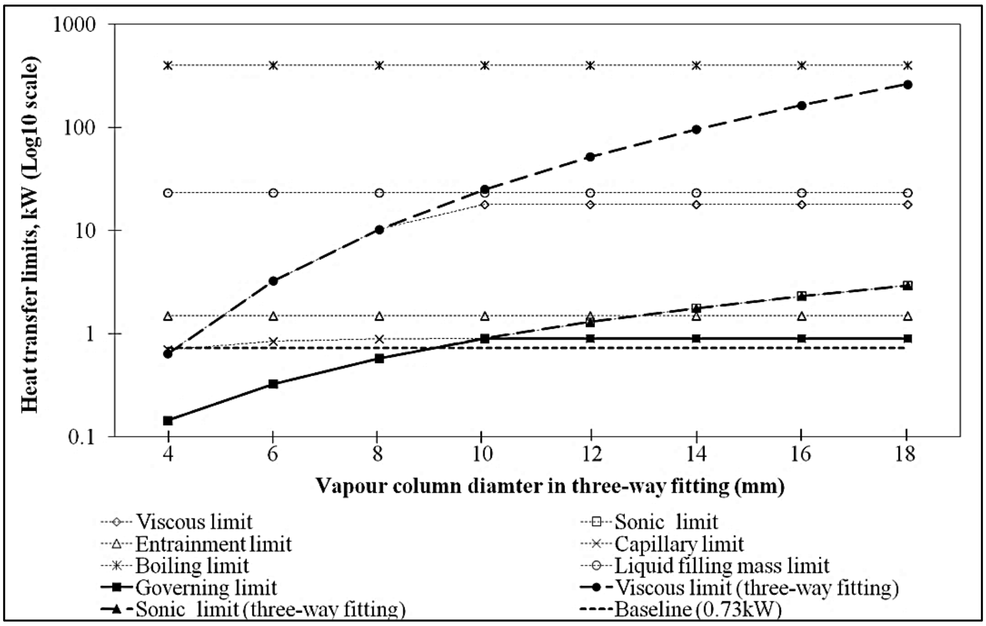

Fig. 3-8: *Impact of vapor column diameter on the heat transfer performance of the LHP* [62]

In this case, the governing limit varied with the different diameter level in the vapor column. The sonic limit, occurring in the three-way fitting, was initially found to be the critical limit, while the vapor column diameter was below 10 mm, whereas the capillary limit became the governing limit when the column diameter was above 10 mm. Through this observation, it was concluded that the minimum vapor column diameter in the three-way fitting should be no less than 10 mm for this LHP operation in order to avoid the overall heat transfer ability being weakened.

(7) Impact of Liquid Filling Mass

While the other loop operating and design parameters remained the same, the correlation between the liquid filling mass and the LHP heat transfer limits is displayed in **Fig. 3-9**. The governing limit was first observed to be the liquid filling mass when the mass level was below 0.01 kg, but it became the capillary limit when the mass level was above 0.01 kg. On the basis of this phenomenon, it was concluded that the minimum liquid filling mass should be more than

0.01 kg for the screen-mesh wick; otherwise, a surface dry-out state would occur within the evaporator.

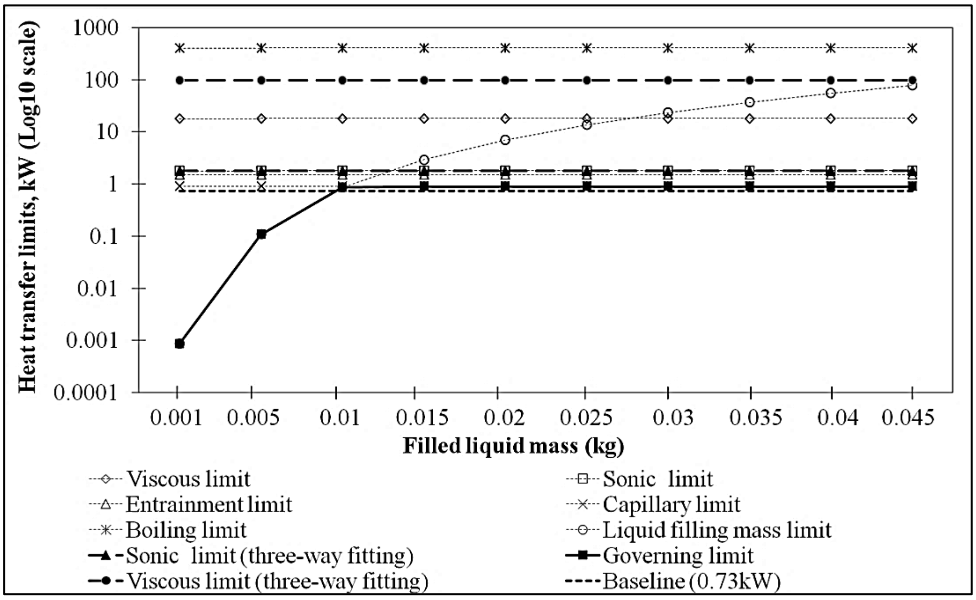

Fig. 3-9: *Impact of liquid filling mass on the heat transfer performance of the LHP* [62]

(8) Impact of Evaporator-to-condenser Height Difference

The capillary limit dominated the heat transfer when the height difference was below 1.1 m, while the entrainment limit (occurring in the heat exchanger) became the governing factor when the elevation difference was above 1.1 m.

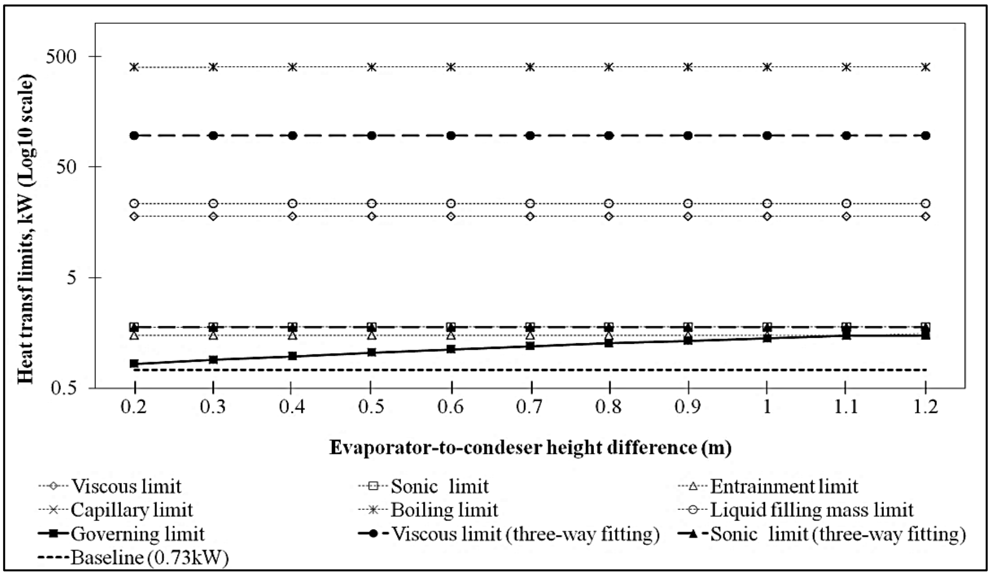

Fig. 3-10: *Impact of evaporator-to-condenser height difference on the heat transfer performance of the LHP* [62]

III.3. Dynamic Model for the Evaluation of System Performance

III.3.1. Modelling Objective for the System Dynamic Performance

The dynamic modelling had the aim of evaluating the performance of the integrated PV/LHP heat pump system in real climatic operational conditions, which are simultaneously affected by several critical factors, i.e., solar radiation, air temperature, air velocity and operating time.

III.3.2. Thermal Fluid Theory and the Associated Mathematical Equations of the System Dynamic Model

For the PV/LHP module-based heat pump water heating system, the transient operational model involved six energy balance equations (as illustrated in **Fig. 3-11**): (1) a heat balance equation for the glazing cover; (2) a heat balance equation for the PV layer; (3) a one-dimensional unsteady-state heat conductance of the fin sheet; (4) a heat balance equation for the LHP operation; (5) heat balance equations for the heat pump cycle and (6) the water tank. To simplify the energy model, the following hypotheses were made:

a. The vertical temperature gradient over the glazing cover was ignored.

b. The ohm electrical losses in the solar cells and PV module are negligible.

c. The heat capacities of the EVA filler (the adhesive for connecting the PV cells and PV glass during lamination) were not included, treating the PV layer as a uniform temperature variation.

d. Heat conduction in the longitudinal direction of the fin sheet was ignored.

e. An isentropic efficiency up to 88% was assumed for the calculation of the compressor power consumption.

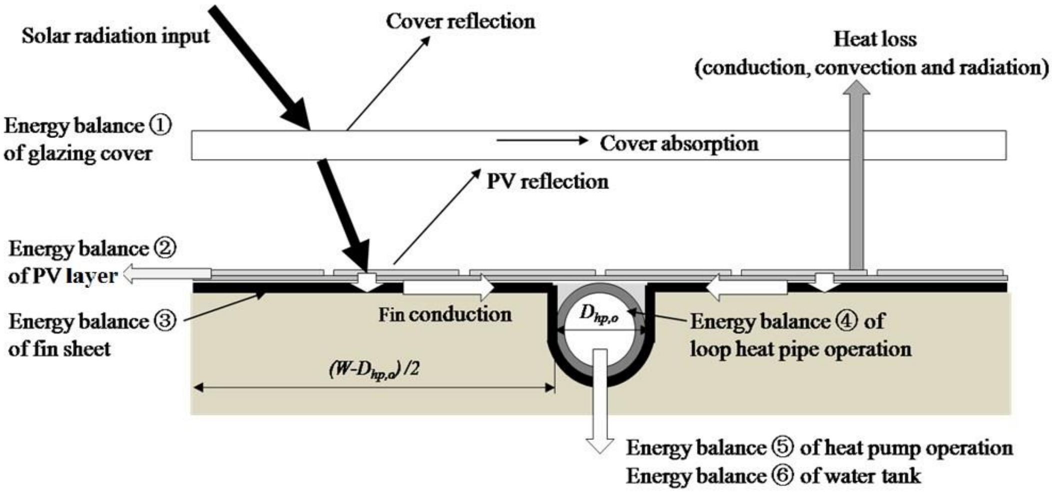

Fig. 3-11: *Schematic of the transient energy balances in the system* [11]

(1) Heat Balance of the Glazing Cover

To describe the time dependence of the heat flows on a single glazing cover, the corresponding energy balance equation is given by [63]

$$\rho_c c_c \delta_c \frac{\partial T_c}{\partial t} = I\alpha_c + \left(h_{c,p-c} + h_{R,p-c}\right)\left(T_p - T_c\right) - \left(h_{c,c-a} + h_{R,c-a}\right)(T_c - T_a) \qquad [3-42]$$

where, ρ_c, c_c and δ_c are respectively the density (kg/m^3), specific heat capacity (J/kg-K) and thickness (m) of the glazing cover; t is the operation time (s); T_c and T_a are respectively the temperatures (K) of glazing cover and ambient air; $h_{c,p-c}$ and $h_{c,c-a}$ are respectively the convective heat transfer coefficients (W/m^2-K) from PV layer to cover and from cover to ambient air; while $h_{R,p-c}$ and $h_{R,c-a}$ are respectively the radiative heat transfer coefficients (W/m^2-K) from PV layer to cover and from cover to ambient air.

For a relatively steady convective air layer exists between the PV absorber surface and the inner glazing cover. Its associated convective heat transfer coefficient, $h_{c,p-c}$, is termed as [64]

$$h_{c,p-c} = \frac{k_{a,p}}{\delta_{a,p}}\left\{1 + 1.446\left(1 - \frac{1708}{Ra_{a,p}cos\theta}\right)^{+}\left[1 - \frac{1708sin^{1.6}(1.8\theta)}{Ra_{a,p}cos\theta}\right] + \left[\left(\frac{Ra_{a,p}cos\theta}{5830}\right)^{0.333}\right]^{+} - 1\right\} \qquad [3-43]$$

where, $k_{a,p}$ is thermal conductivity of air gap at the average temperature of PV layer and inner cover surface (W/m-k); $\delta_{a,p}$ is the PV layer to glazing cover distance (m); θ is the collector slop (degree); the bracket with plus means zero and positive values only; $Ra_{a,p}$ is the Rayleigh number of the air gap at PV layer and inner cover surface.

A simple accurate formula for optimum tilt angle for all over the world was recently proposed by Camelia Stanciu et al. [65]

$$\theta = L_m - \delta_m \qquad [3-44]$$

Where L_m is the longitude and δ_m is the sun declination (degree).

$$Ra_{a,p} = \frac{g\left(T_p - T_c\right)\delta_{a,p}^3}{\nu_{a,p}^2 T_{a,m}} Pr_{a,p} \qquad [3-45]$$

where, g is the gravity acceleration (m/s^2) and νa is kinematic viscosity of air at the PV and inner cover surface (m^2/s); $Pr_{a,p}$ is the Prandtl number of the air gap at PV layer and inner cover surface, which is assumed to be independent of temperature and taken equal to 0.7; $T_{a,m}$ is the average air temperature of PV layer and inner cover surface which is

$$T_{a,m} = \frac{\left(T_p + T_c\right)}{2} \qquad [3-46]$$

where, T_p and T_c are respectively the average temperatures (K) of PV layer and inner cover surface.

Converting the radiation transfer into the equivalent convective one, a radiation-relevant factor, $h_{R,p\text{-}c}$, is expressed by

$$h_{R,p-c} = \frac{\sigma\left(T_p + T_c\right)\left(T_p^2 + T_c^2\right)}{1/\varepsilon_p + 1/\varepsilon_c - 1} \qquad [3-47]$$

where, ε_p and ε_c are emissivity of the PV layer and inner cover surface; σ is the Stefan–Boltzman constant (5.6679×10^{-8} W/m^2-K^4).

For a surface exposed to the outside wind, the convective coefficient could be calculated using the Klein equation [66], addressed below

$$h_{c,c-a} = \frac{8.6V^{0.6}}{L^{0.4}} \qquad [3-48]$$

where, V is the wind speed (m/s); L is the characteristic length of the collector (m). The minimum convective coefficient for a wind-exposed surface is considered to be 5 W/m^2-K [66]; if the above calculation gives a lower value, this should be replaced by the minimum value of 5.

Since the temperature of the sky has little impact on the calculation result, it is usually represented by the air temperature, thus

$$h_{R,c-a} = \varepsilon_c \sigma (T_c + T_a)\left(T_c^2 + T_a^2\right) \qquad [3-49]$$

(2) Heat Balance of the PV Layer

The energy balance equation for the combined PV lamination is [63]

$$\rho_p c_p \delta_p \frac{\partial T_p}{\partial t} = \left[I(\tau_c \alpha)_b \left(1-\beta_p\right) + I(\tau_c \alpha)_p \beta_p - q_e\right] - \frac{T_p - T_f}{R_{p-f} A_p} - \left(h_{c,p-c} + h_{R,p-c}\right)\left(T_p - T_c\right) \qquad [3-50]$$

where, ρ_p, c_p and δ_p are respectively the average density (kg/m^3), specific heat capacity (J/kg-K) and thickness (m) of the PV layer; T_p and T_f are average the temperatures (K) of PV layer and fin sheet; $(\tau_c\alpha)_b$ and $(\tau_c\alpha)_p$ are the respectively the transmittance-absorption coefficients of baseboard and PV layer; β_p is the packing factor of PV layer; R_{p-f} is the overall thermal resistances (K/W) from PV cells to fin sheet; A_p is the absorbing area of PV layer (m^2).

The overall transient solar transmittance for a single cover becomes [64]

$$\tau_c = \frac{\tau_{c,\alpha}}{2}\left\{\frac{1-r_\parallel}{1+r_\parallel}\left[\frac{1-r_\parallel}{1-\left(r_\parallel \tau_{c,\alpha}\right)^2}\right] + \frac{1-r_\perp}{1+r_\perp}\left[\frac{1-r_\perp}{1-\left(r_\perp \tau_{c,\alpha}\right)^2}\right]\right\} \qquad [3-51]$$

In above equation, the transmittance due to absorption, $\tau_{c,\alpha}$ is written as

$$\tau_{c,\alpha} = exp\left[-\frac{K\delta_c}{cos(\theta_2)}\right] \qquad [3-52]$$

And the refraction angle of direct solar beam, θ_2 (rad), is given

$$\theta_2 = sin^{-1}\left(\frac{sin\theta_1}{n_g}\right) \qquad [3-53]$$

where, n_g is the ratio of the refraction index and is typically 1.526 for glass. θ_1 is the incidence angle (rad) striking the glazing surface, and for a south-facing tilted plane in the Northern Hemisphere, the expression for the incidence angle is given by [64]

$$cos(\theta_1) = sin(L_m - \theta)sin(\delta_m) + cos(L_m - \theta)cos(\delta_m)cos(h_m) \qquad [3-54]$$

The thermal resistance from PV cells to the fin sheet is calculated as

$$R_{p-f} = R_p + R_{EVA} + R_{ei} = \frac{\delta_p}{k_p A_p} + \frac{\delta_{EVA}}{k_{EVA} A_{EVA}} + \frac{\delta_{ei}}{k_{ei} A_{ei}} \qquad [3-55]$$

where, R_p, R_{EVA} and R_{ei} are respectively the thermal resistances (K/W) of PV cells, EVA layer and electrical insulation; k_p, k_{EVA}, k_{ei}, δ_p, δ_{EVA}, and δ_{ei} are respectively the thermal conductivities (W/m-K) and thickness (m) of PV layer, EVA layer and electrical insulation.

The corresponding electricity output per unit area, q_e (W/m^2), is defined by

$$q_e = I(\tau_c \alpha)_p \beta_p \eta_p \left[1 - \beta_{PV}\left(T_p - T_{rc}\right)\right] \qquad [3-56]$$

(3) Heat Balance of the Fin Sheet

The time-dependent heat conductance of the PV-based fin sheet can be tackled as a typical one-dimensional unsteady-state heat transfer on an infinite flat plate. The fin sheet can be divided into various small segments depending on the specific sheet size and differential step space, shown in **Fig. 3-22**. The temperature profile is thereby assumed to be symmetrical with respect to the LHP evaporator location and its heat balance equations are expressed as [63]

$$\begin{cases} \rho_f c_f \delta_f \dfrac{\partial T_f}{\partial t} = k_f \delta_f \dfrac{\partial^2 T_f}{\partial x^2} + \dfrac{T_p - T_f}{R_{p-f} A_p} - \dfrac{T_f - T_a}{R_{f-a} A_{fs} + 1/h_a A_{fe}} & [3-57] \\ \\ \rho_f c_f \delta_f \dfrac{\partial T_{f,11}}{\partial t} = \dfrac{T_{p,11} - T_{f,11}}{R_{p-f} A_p} - \dfrac{T_{f,11} - T_{hp,w}}{R_{f-hp} A_{fc}} - \dfrac{T_{f,11} - T_a}{R_{f-a} A_{fs}} & [3-58] \end{cases}$$

where, ρ_f, c_f and δ_f are respectively the average density (kg/m^3), specific heat capacity (J/kg-K) and thickness (m) of fin sheet; T_f and $T_{hp,w}$ are the average temperatures (K) of fin sheet and heat-pipe wall surface; $T_{p,11}$ and $T_{f,11}$ are the temperatures (K) of PV layer and fin sheet at the 11 node; k_f is the thermal conductivity of fin sheet (W/m-K); x is the lengh along the fin width direction (m); R_{f-a} and R_{f-hp} are the overall thermal resistances (K/W) from fin sheet to ambient air and from fin sheet to heat pipe; h_a is the convective coefficient of surrounding air (W/m^2-K); A_{fc}, A_{fs} and A_{fe} are respectively the central fin area (m^2), insulation areas around fin sheet (m^2) and the edge area of fin sheet (m^2).

The initial temperature and boundary conditions are described as

$$\begin{cases} T(x,0) = T_{f,i}^{0} \,, & t = 0 \\ -k_f \left.\dfrac{\partial T}{\partial x}\right|_{x=0} = h_a\left(T_{f,0} - T_a\right) \,, & t > 0 \\ T\left(\dfrac{W}{2}, t\right) = T_{f,11} \,, & t > 0 \end{cases} \qquad [3-59]$$

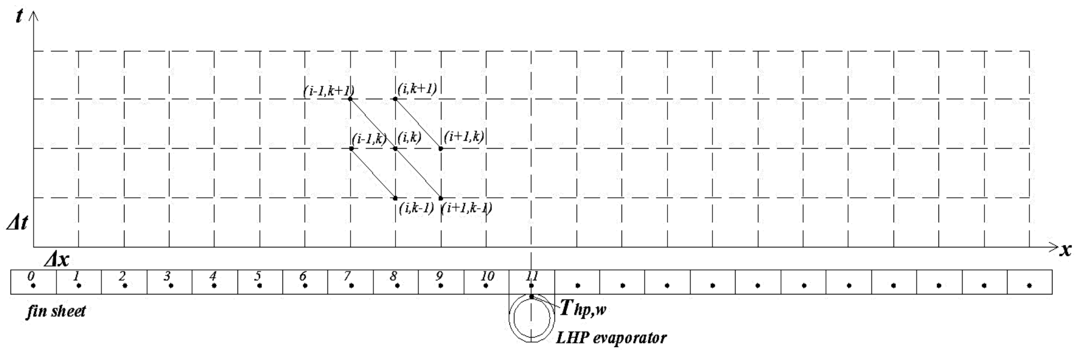

Fig. 3-12: *Grid meshing for the fin sheet along the width* [11]

The thermal resistances of the insulation bodies separating the fins from the air and beneath the fins are, respectively, written as

$$R_{f-a} = \frac{\delta_{fs}}{k_{fs} A_{fs}} \qquad [3-60]$$

$$R_{f-hp} = \frac{\delta_{f}}{k_{f} A_{fc}} \qquad [3-61]$$

where, k_{fs} and δ_{fs} are the thermal conductivity (W/m-K) and thickness (m) of the insulation around fin sheet respectively.

(4) Heat Balance of the LHP

The time-dependent heat transfer variation within the loop heat pipe is [55]

$$\frac{1}{4}\pi\left(D_{hp,o}^{2}-D_{hp,in}^{2}\right)\rho_{hp}c_{hp}\delta_{hp}\frac{\partial T_{hp,w}}{\partial t}=\frac{T_{f,11}-T_{hp,w}}{R_{f-hp}A_{fc}}-\frac{T_{hp,w}-T_{r,m}}{R_{hp,r}}-\frac{T_{hp,w}-T_{a}}{R_{hp-a}} \quad [3-62]$$

where, ρ_{hp}, c_{hp} and δ_{hp} are respectively the average density (kg/m^3), specific heat capacity (J/kg-K) and thickness (m) of LHP evaporation section; $T_{r,m}$ is the mean temperature (K) of refrigerant; R_{hp-a} is the thermal resistance between the heat pipe transportation line and the ambient air (K/W), given by

$$R_{hp-a}=\frac{ln\left(D_{hp,o}/D_{hp,in}\right)}{2\pi L_{hp}k_{hp}}+\frac{1}{h_{a}A_{hp}} \quad [3-63]$$

Thermal resistance between the LHP evaporation section and the heat-pump refrigerant, R_{hp-r} (K/W), is considered as the overall value that occurring in different components, including heat pipe wall ($R_{hp,w}$), wick structure (R_{wi}), liquid film (R_{lf}), heat exchanger (R_{hx}) and refrigerant flow (R_r). Other resistances, such as those of the liquid-vapor interface at the wick structure and the vapor flow in the vapor line, can be ignored due to their much smaller values calculated in the previous section.

$$R_{hp-r}=R_{hp-w}+R_{wi}+R_{lf}+R_{hx}+R_{r} \quad [3-64]$$

i. Heat Pipe Wall, R_{hp-w}

$$R_{hp-r}=\frac{ln\left(D_{hp,o}/D_{hp,in}\right)}{2\pi L_{hp,e}k_{hp}} \quad [3-65]$$

where, $D_{hp,o}$, $D_{hp,in}$, $L_{hp,e}$ and k_{hp} are the outer diameter (m), inner diameter (m), length (m) and thermal conductivity of the absorbing heat pipe (W/m-K).

ii.Thermal Resistance of the Wick Structure, R_{wi}

The inner surface of the heat pipe wall is attached to the mesh wick, which causes a certain resistance in heat transfer; this part of the resistance is addressed as

$$R_{wi}=\frac{ln\left(D_{hp,in}/D_{v,e}\right)}{2\pi L_{hp,e}k_{wi}} \quad [3-66]$$

where, k_{wi} is the effective thermal conductivity of wick structure (W/m-K).

$$k_{wi}=(k_{owi}+k_{iwi})/2 \quad [3-67]$$

where, k_{owi} , k_{iwi} are the effective thermal conductivity of outer/inner wick structure (W/m-K),

$$k_{owi} = \frac{k_l\left[(k_l + k_s) - (1 - \varepsilon_{owi})(k_l - k_s)\right]}{\left[(k_l + k_s) + (1 - \varepsilon_{owi})(k_l - k_s)\right]} \qquad [3-68]$$

where, ε_{owi} is the porosity of outer mesh screen layer, k_l and k_s are the thermal conductivities of liquid and wick structure (W/m-K). The effective thermal conductivity of the inner screen layer can be similarly obtained from above equation

$$\varepsilon_{owi} = 1 - \frac{1.05\pi N_{owi} D_{owi}}{4} \qquad [3-69]$$

iii. Thermal Resistance of the Condensed Liquid Film, R_{lf}

The condensed liquid film is evenly distributed on the surface of the condensing heat exchanger (on the heat pipe side) and its associated flow resistance is [63]

$$R_{lf} = \frac{ln\left[D_{hx,in}/\left(D_{hx,in} - 2\delta_{lf}\right)\right]}{2\pi L_{lf} k_{lf} (N_{hx}/2 - 1)} \qquad [3-70]$$

where, δ_{lf}, L_{lf} and k_{lf} are the thickness (m), length (m) and thermal conductivity (W/m-K) of the liquid film; $D_{hx,in}$ is the internal hydraulic diameter of heat exchanger (m); N_{hx} is the number of heat exchanger plates.

iv.Thermal Resistance of the Heat-exchanging Plate, R_{hx}

The equivalent thermal resistance of the heat-exchanging plate is derived as

$$R_{hx} = \frac{ln\left(D_{hx,o}/D_{hx,in}\right)}{2\pi k_{hx} (H_{hx}/2)(N_{hx}/2 - 1)} \qquad [3-71]$$

where, k_{hx} is the thermal conductivity of heat exchanger plate (W/m-K).

v.Thermal Resistance of the Heat Pump Refrigerant, R_r

The refrigerant in the heat pump cycle passes across the channels of the condensing heat exchanger (on the refrigerant side), where it is evaporated into vapor. This process involves turbulent and forced convection heat transfer, and its associated thermal resistance is [63]

$$R_r = \frac{1}{h_r A_{hx,r} (N_{hx}/2)} \qquad [3-72]$$

where, $A_{hx,r}$ is the internal surface area of refrigerant flow in each heat exchanging channel (m^2); h_r is the heat transfer coefficient (W/m^2-K) of two phase refrigerant flow for each heat-exchanging channel, which is given by

$$h_r = h_{r,l}\left[(1-x_r)^{0.8} + \frac{3.8x_r^{0.76}(1-x_r)^{0.04}}{Pr_r^{0.38}}\right] \qquad [3-73]$$

where, x_r, is the saturation of refrigerant; $h_{r,l}$, is heat transfer coefficient of the liquid refrigerant (W/m^2-K).

$$h_{r,l} = \frac{Nu_r k_{r,l}}{D_{hx,in}} \qquad [3-74]$$

where, $k_{r,l}$ is the thermal conductivity of liquid refrigerant (W/m-K). The Nusselt number of refrigerant can be derived from the Dittus-Boelter equation

$$Nu_r = 0.023 Re_{r,l}^{0.8} Pr_{r,l}^{0.4} \qquad [3-75]$$

$$Re_{r,l} = \frac{m_r(1-x_r)D_{hx,in}}{\mu_{r,l}(N_{hx}/2)N_{hp}A_{hx,r}} \qquad [3-76]$$

where, $\mu_{r,l}$ and m_r are respectively the mean dynamic viscosity (kg/m-s) and mass flow rate (kg/s) of liquid refrigerant within each heat-exchange channel.

$$Pr_{r,l} = \mu_{r,l} c_{pr,l}/k_{r,l} \qquad [3-77]$$

where, $c_{pr,l}$ is specific heat of liquid refrigerant at a constant pressure (J/kg-K).

(5) Heat Balances of the Heat Pump and Water Tank

The solar heat delivered to the heat pump operation is theoretically given by

$$\frac{\partial\left(M_r H_{r,e}\right)}{\partial t} = \frac{T_{hp,w} - T_{r,m}}{R_{hp-r}} - \frac{T_{hp,w} - T_a}{R_{hp-a}} \qquad [3-78]$$

where, M_r is the mass of refrigerant (kg); $H_{r,e}$ is the enthalpy of refrigerant in the evaporation section (J/kg);

With consideration of the additional compressor work input, the condensation heat expelled from the heat pump is defined as [67, 68]

$$M_w c_w \frac{\partial T_w}{\partial t} = \frac{\partial\left(M_r H_{r,c}\right)}{\partial t} - \frac{T_w - T_a}{R_{w-a}} \qquad [3-79]$$

where, M_w and c_w are the mass (kg) and special heat capacity (J/kg-K) of water; $H_{r,c}$ is the enthalpy of refrigerant in the condensation section (J/kg); T_w is the mean temperature of water in the tank (K); R_{w-a} is the equivalent thermal resistance between the water and the ambient air (K/W). This amount of heat is fully transported into the tank water.

$$R_{w-a} = \frac{ln\left(D_{ws,o}/D_{ws,in}\right)}{2\pi L_{ws} k_{ws}} + \frac{1}{h_a A_{ws}} \qquad [3-80]$$

where, $D_{ws,o}$, $D_{ws,in}$, L_{ws}, k_{ws} and A_{ws} are respectively the outer/inner diameters (m), length (m), thermal conductivity (W/m-K) and surface area (m^2) of water tank insulation.

Once the evaporation and the condensation temperatures are set constantly, the mass flow rate is considered as the primary parameter that determines the thermodynamic process in the heat pump, which can be congruously treated as a special variable in despite of using of the fixed or variable speed compressor: (1) the fixed speed compressor varies the mass flow rate by simply switching on or off during a certain operational period; (2) the variable speed compressor adjusts its motor speed automatically to affect the mass flow rate transiently.

(6) Grouped differential equations set-up

To resolve the above equations using a numerical method, the differential equations can be rewritten in the formats of the MATLAB's "*ode15s*" and "*pdepe*" solvers. The MATLAB "*pdepe*" solver is normally applied for the initial-boundary value problems to solve the parabolic and elliptic partial differential equation (PDE) systems in one space variable "*x*" and time "*t*". This solver converts the PDE into ordinary differential equation (ODE) using a second-order accurate spatial discretization based on a set of nodes, which is recognized as a classical FEM method. The time integration is completed with the "*ode15s*" solver, which is a variable order solver to resolve the algebraic equations according to the backward differentiation formulas.

To use the "*ode15s*" solver, the grouped ODE's is needed to be rewritten in below format [69]

$$
\begin{cases}
dy = \left[T_c; T_p; T_{f,11}; T_{hp,w}; m_r; T_w\right] = [y(1); y(2); y(3); y(4); y(5); y(6)] \\
dy(1) = \left\{I\alpha_c + \left(h_{c,p-c} + h_{R,p-c}\right)[y(2) - y(1)] - \left(h_{c,c-a} + h_{R,c-a}\right)\left[y(1) - T_a\right]\right\}/\rho_c c_c \delta_c \\
dy(2) = \left\{\begin{matrix} \left[I(\tau_c\alpha)_b\left(1 - \beta_p\right) + I(\tau_c\alpha)_p\beta_p - Q_e\right] \\ -[y(2) - y(3)]/R_{p-f}A_p - \left(h_{c,p-c} + h_{R,p-c}\right)[y(2) - y(1)] \end{matrix}\right\}/\rho_p c_p \delta_p \\
dy(3) = \left\{[y(2) - y(3)]/R_{p-f}A_p - [y(3) - y(4)]/R_{f-hp}A_{fc} - \left[y(3) - T_a\right]/R_{f-a}A_{fs}\right\}/\rho_f c_f \delta_f \\
dy(4) = \left\{\begin{matrix} \frac{\pi}{4}[y(3) - y(4)]/R_{f-hp}A_{fc} \\ -\left[y(4) - T_{r,m}\right]/R_{hp-r} - \left[y(4) - T_a\right]/R_{hp-a} \end{matrix}\right\}/\left(D_{hp,o}^2 - D_{hp,in}^2\right)\rho_{hp}c_{hp}L_{hp} \\
dy(5) = \left\{\left[y(4) - T_{r,m}\right]/R_{hp-r} - \left[y(4) - T_a\right]/R_{hp-a}\right\}/H_{r,e} \\
dy(6) = \left\{y(5)H_{r,c} - \left[y(6) - T_a\right]/R_{w-a}\right\}/M_w c_w
\end{cases}
\quad [3-81]
$$

To use the "*pdepe*" solver, the PDE function, initial and boundary conditions should satisfy the forms below [69]

$$
\begin{cases}
C\left(x, t, T, \frac{\partial T}{\partial x}\right)\frac{\partial T}{\partial t} = x^{-m}\frac{\partial}{\partial x}\left[x^m f\left(x, t, T, \frac{\partial T}{\partial x}\right)\right] + s\left(x, t, T, \frac{\partial T}{\partial x}\right) \\
T(x, t_0) = T_0(x) \\
p(x, t, T) + q(x, t)f\left(x, t, T, \frac{\partial T}{\partial x}\right) = 0 \\
t \in \left[t_0, t_f\right], x \in [a, b]
\end{cases}
\quad [3-82]
$$

In this case, the dedicated PDE can be rewritten as follows

$$\begin{cases} \rho_f c_f \delta_f \dfrac{\partial T_f}{\partial t} = k_f \delta_f x^0 \dfrac{\partial}{\partial x}\left(x^0 \dfrac{\partial T_f}{\partial x}\right) + \left[\dfrac{T_p - T_f}{R_{p-f} A_p} - \dfrac{T_f - T_a}{R_{f-a} A_{fs} + 1/h_a A_{fe}}\right] \\ T(x,0) = T_f^0 \\ h_a\left(T_{f,0} - T_a\right) + k_f \dfrac{\partial T_f}{\partial x}\Big|_{x=0} = 0 \\ T_{f,11} - T_f\left(\dfrac{W}{2}, t\right) \\ t \in [0, end], x \in \left[0, \dfrac{W}{2}\right] \end{cases} \qquad [3-83]$$

The time step size, *Δt,* and the space step size, *Δx,* are chosen to get convergence with maximum precision. As the temperature profile of the fin sheet is assumed to be symmetrical at two sides of the LHP evaporator in the center, there are then only considered to be 11 elements from the left-hand edge to the fin center along the fin width, as shown in **Fig. 3-22**.

(7) Module Efficiencies

The overall energetic efficiency is the ratio of the generated electricity and heat to the incident solar radiation striking the module. It is yielded from the first law of thermodynamics and indicates the percentage of the energy converted from solar radiation. The descriptions of the energetic efficiencies are

$$\eta_e = \frac{\int_{t_0}^{t_{k+1}} Q_e dt}{\int_{t_0}^{t_{k+1}} A_m I dt} \qquad [3-84]$$

$$\eta_{th} = \frac{\int_{t_0}^{t_{k+1}} Q_{th} dt}{\int_{t_0}^{t_{k+1}} A_m I dt} \qquad [3-85]$$

$$\eta_0 = \eta_e + \eta_{th} \qquad [3-86]$$

III.3.3. Algorithm for the Dynamic Model Development and Operation

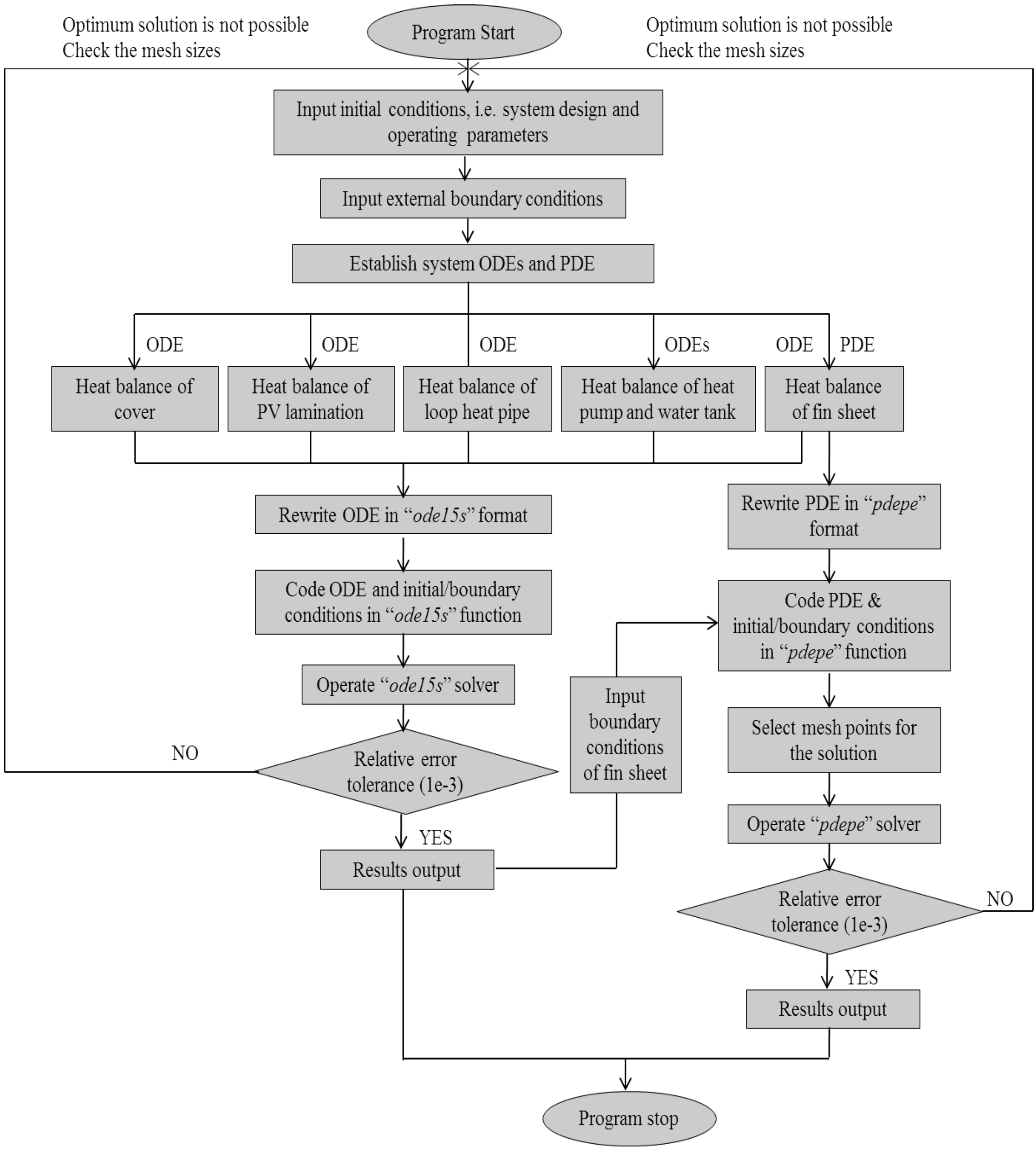

Fig. 3-13: *Flow chart for calculating the Dynamic Model*

III.4. Chapter Conclusion

This chapter investigated the theory behind the LHP and the PV/LHP heat pump system. Two computer simulation models were built for the LHP heat transfer capacity and for the system dynamic performance.

In the LHP analytical model, six operational limits were considered, including viscous, sonic, entrainment, capillary, boiling and liquid filling mass. The impact of several of the operational and geometric parameters of the LHP on its heat transfer limits was investigated.

Through the established dynamic model, evaluation of the PV/LHP heat pump system could, therefore, be conducted in real climate conditions. A detailed discussion will be provided in Chapter 4.

Chapter IV:

Results & Findings

IV. Results & Findings

IV.1. Chapter Introduction

This chapter will present and discuss results of dynamic model simulation in real climatic operational conditions. Plots of real data used of the region of Bouzzereah, Algiers – Algeria dated on 03 January 2015, this data was provided by CDER Alger (Centre de Development des Energies Renouvelable) of real measurements, as shown in **Fig. 4-1** and **Fig. 4-2**.

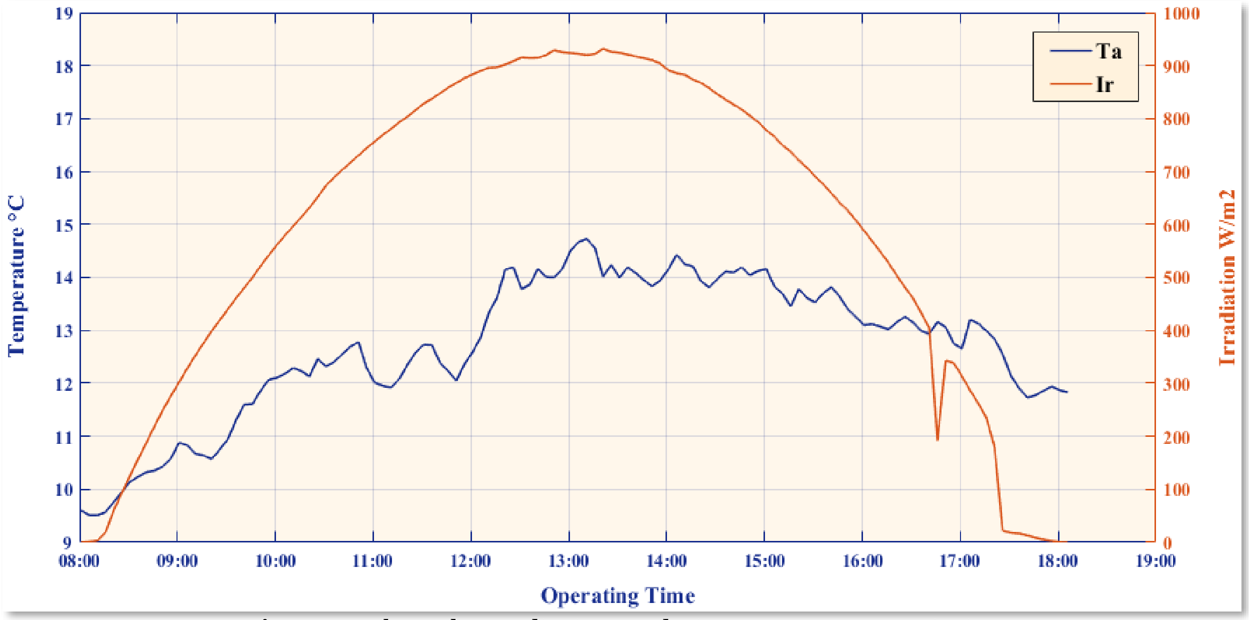

Fig. 4-1: *The solar radiation and air temperature variation*

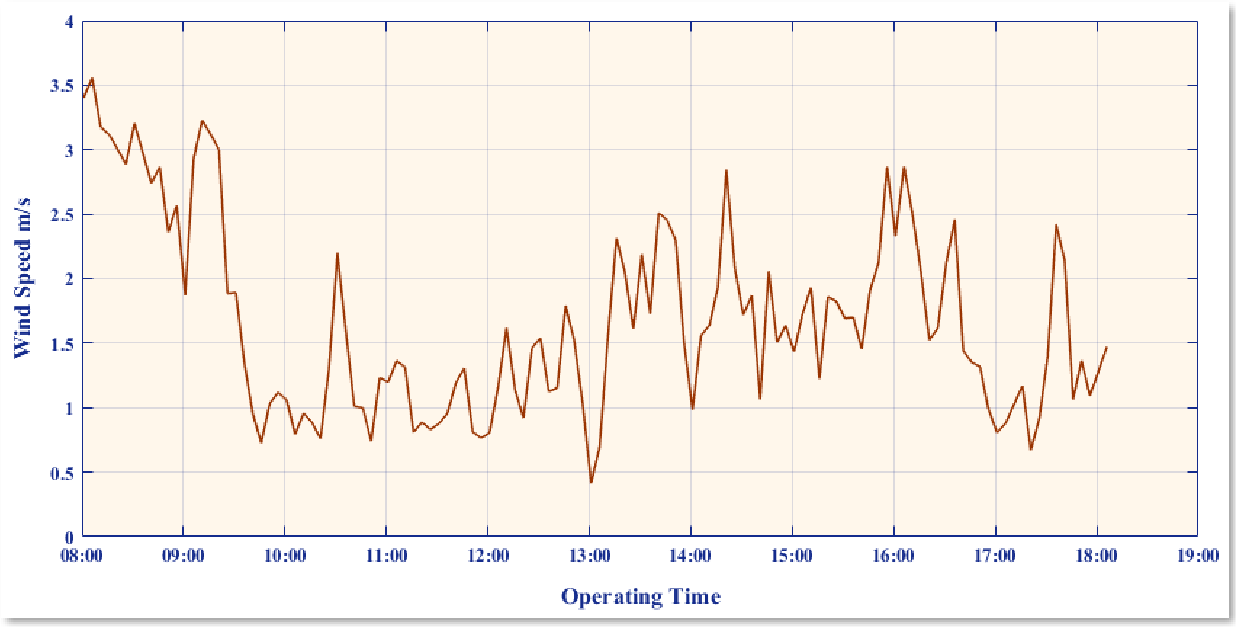

Fig. 4-2: *Wind Speed variation*

IV.2. Results and Discussion

The main results obtained by the dynamic computer model have shown good trend coherence is noticed with previous published simulation results. Comparison with Zhang et al. [11] model is presented in **Table. 4-1**.

Table 4-1: *Average Data and Results comparison*

Date	T_a °C	I_r W	Wind m/s	Q_e W	Q_{th} W	Q_w W	η_e %	η_{th} %	η_0 %
03/01/2015	12.7	589.58	1.67	**36.62**	150.43	181.33	**11.30**	53.41	64.70
21/11/2011 Zhang et al.	15.28	525.23	-	**29.91**	122.87	146.86	**9.23**	38.76	47.99

IV.2.1. Temperature distribution

Variation of the temperatures in different system components over the day duration is presented in **Fig. 4-3**, it was found that all temperature values for the glazing cover, PV layer, central fin sheet and heat pipe presented the similar variation trend, giving the up-rising trend in morning and down-falling trend in afternoon; while the temperature of the tank water grew continuously throughout the day duration, starting at 9.6 °C and ending at 60.8 °C.

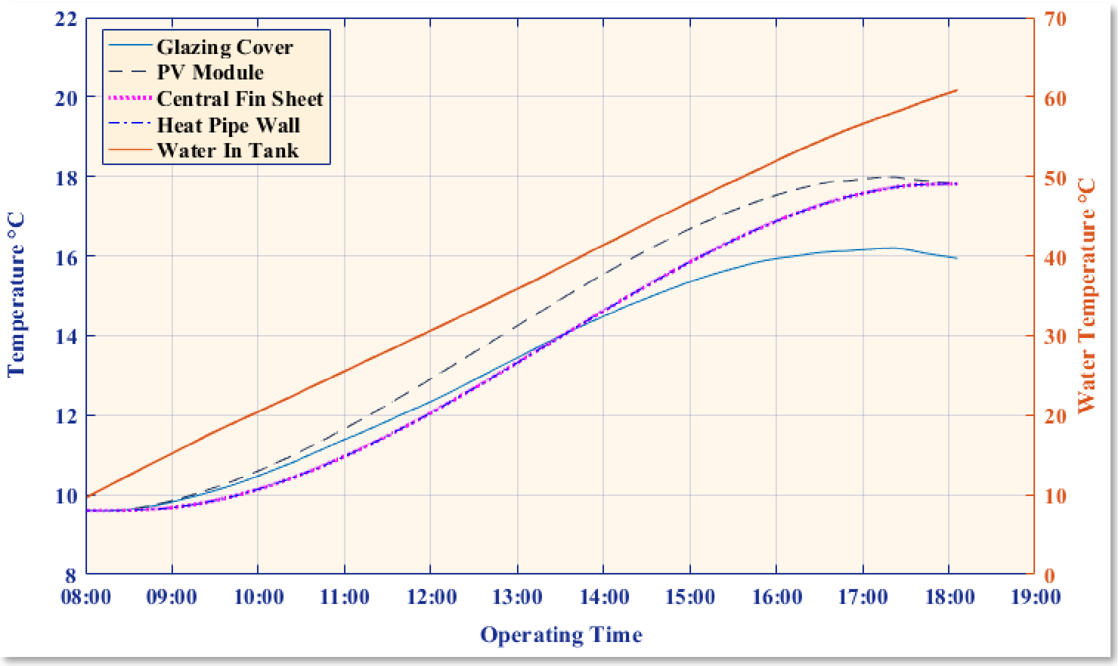

Fig. 4-3: *Temperature distribution in PV/LHP components.*

Also, to be noticed the slight temperature difference between PV layer (Tp_{avg}=14.2 °C) and central fin sheet ($Tf11_{avg}$=15.4 °C) were fully matched in the morning and the end of day, while the maximum shift of 0.9 °C caused by fast heat accumulation in PV layers, was reached at midday, this is clearly owned to the effect of thermally enhanced EVA and the high conductivity of Al-Alloy baseboard. A complete match between the temperatures of central fin sheet and heat pipe wall is reflecting the high heat removal performance of LHP.

IV.2.2. PV/LHP module's electrical output and efficiency

The average electrical output and the corresponding solar electrical efficiency were 36.62 W and 11.30 %. The variation of the module's electrical output was found to be similar to that of the solar radiation, presenting a gradually increasing trend in morning and decreasing trend in afternoon; while the peak electrical output occurred at the noon time. The solar electrical efficiency was found to have a variation trend similar to the transmittance of glazing cover, relatively fast increase in morning from 08:00 to 10:00, slightly slower decrease in late afternoon from 16:00 to 18:00, and remain a relatively stable state in the rest of the day time. This variation trend was largely affected by solar radiation and the corresponding incidence angle.

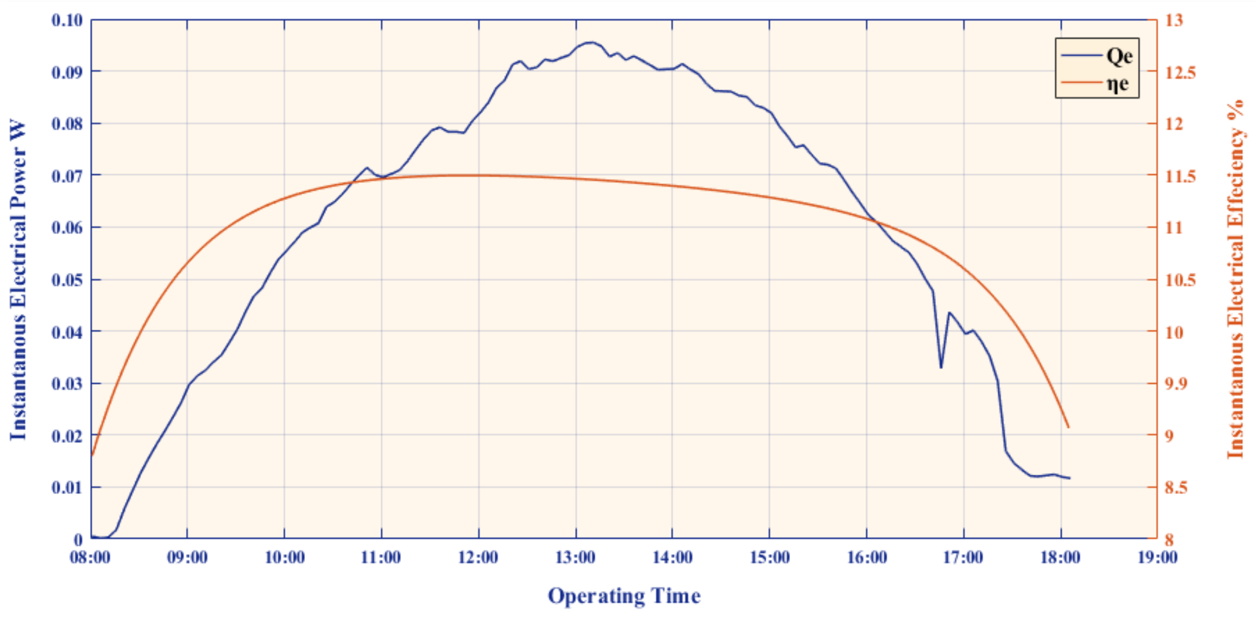

Fig. 4-4: *Instantaneous Electrical Output and Efficiency Variation.*

It is known that larger solar radiation and smaller incidence solar beam angle would result in increased solar energy absorption and thus increased solar electrical output, which is the situation for noon time operation. It is also known that the solar electrical efficiency would change at the opposite trend to the solar incidence angle and at the consistent trend to the PV cells' temperature. So, choosing the optimum tilt angle would increase the duration of small incidence angle of solar beams during the day which is the case in above figure except in the sunshine and sunset times were high incidence angle is encountered.

IV.2.3. PV/LHP module's thermal output and efficiency

Variations of the solar thermal output of the PV/LHP module and the corresponding thermal efficiency over the day duration are presented in **Fig. 4-5**. The average solar heat output of the module and the corresponding solar thermal efficiency were 150.42 W and 53.41%. The thermal output increased slowly in morning and decreased quickly in afternoon. Similar to the situation for the solar electrical output, the solar radiation and incidence angle imposed significant influences to the module's solar thermal output.

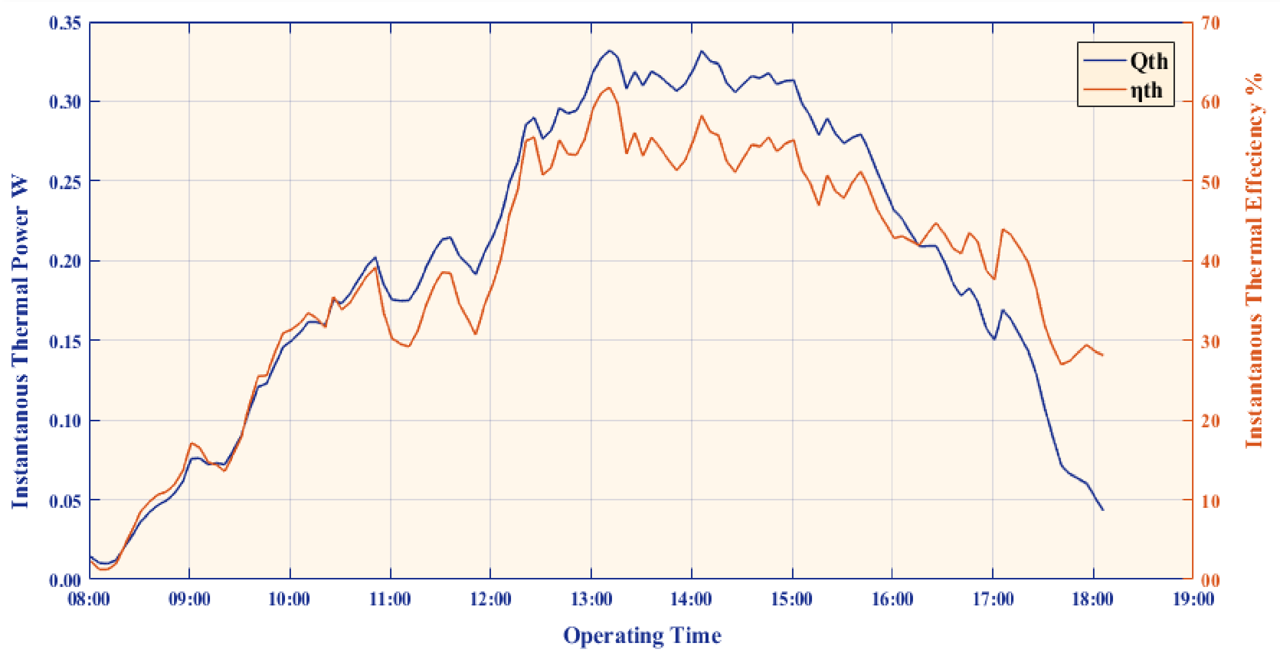

Fig. 4-5: *Instantaneous Thermal Output and Efficiency Variation.*

Different from the situation for the solar electrical output, the wind speed and ambient temperature have also become factors impacting onto the module's heat output; low ambient temperature and higher wind speed (average of 2.25 m/s from 08:00 to 10:00) was noticed in the early morning contributed in high heat loss resulting in a slow growing trend in the morning. Around midday wind speed was relatively low with higher ambient temperature being built, led to reduced convective coefficient and temperature difference between the module's surface and ambient which caused reduced heat loss. As the wind speed was moderate and ambient temperature presented a continuously growing trend, the heat loss from the module's surface to ambient was becoming smaller and smaller during a daytime operation and as a result, the module's net thermal output was slightly higher than in the morning until late afternoon close to sunset time were higher incidence angle caused a quick down-falling process during afternoon.

IV.2.4. Cooling effectiveness & Total efficiency behavior

Correlation between Cooling effectiveness (T_p-T_a) and Total efficiency (η_e+η_{th}) is shown in **Fig. 4-6**. It was noticed that the total efficiency has on opposite variation trend to T_p-T_a and this is a coherent behavior as both electrical and thermal outputs would increase as well as the temperature of PV layer is closer to ambient temperature owing to reduced heat loss and increased PV electrical performance with cooling down.

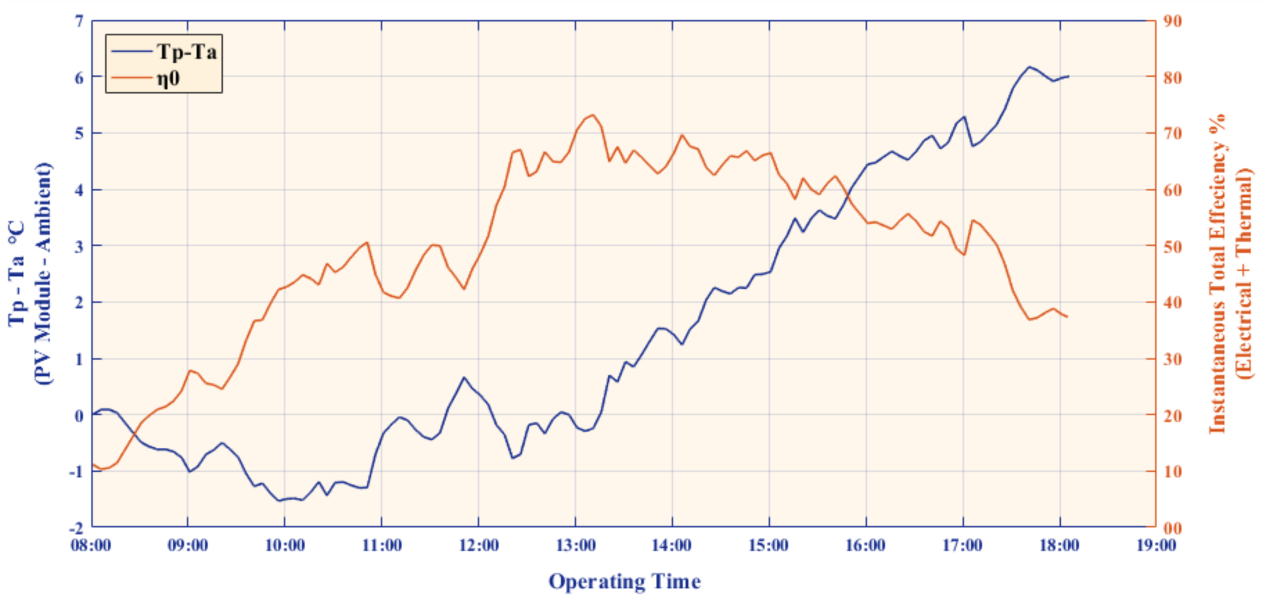

Fig. 4-6: *Cooling effectiveness & Total efficiency behavior.*

IV.2.5. Temperature Distribution Profile in Fin Sheet at Fixed Time

At a single time point, the temperature variation along the fin width tended to have more or less a ‘V’ shape-like, with the minimum value occurring at the central line and the maximum value at the fin edge line.

(1) At 08:00

As shown in **Fig. 4-7**, the temperature profile looks like a straight horizontal line at 9.6 °C which is the ambient temperature at 08:00, this profile is explained by the fact that the LHP did not start yet as the working fluid inside heat pipe (water) needs a minimum of heat to reach the evaporation temperature 10 °C.

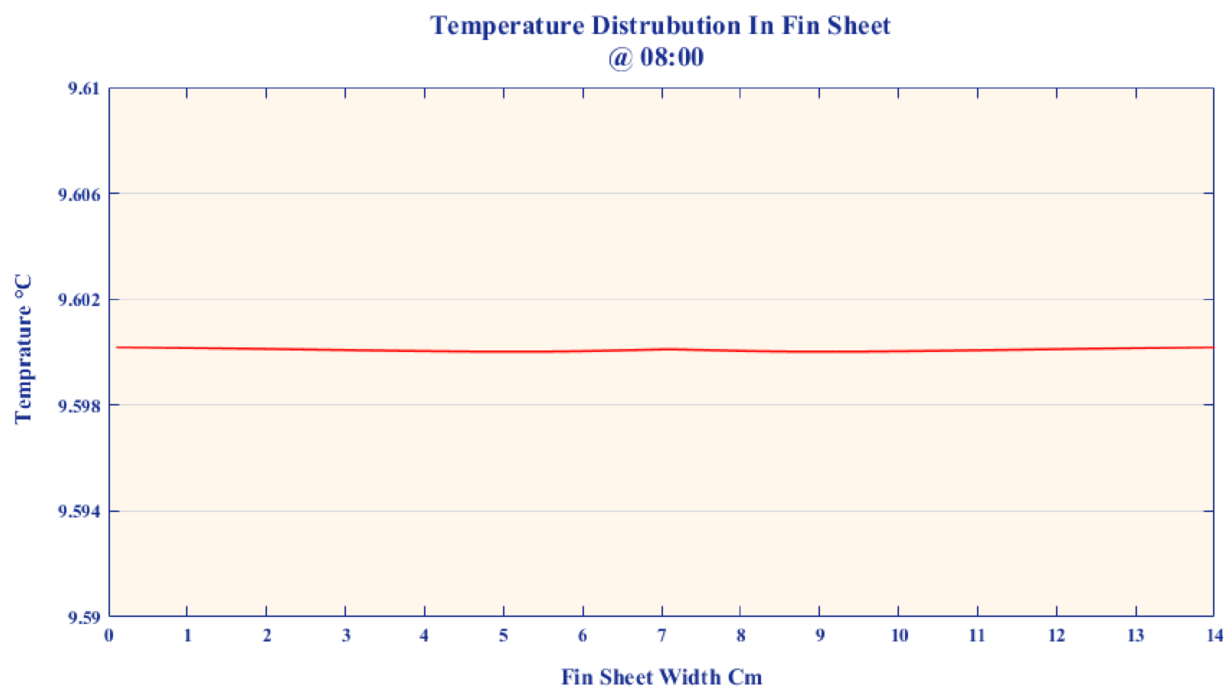

Fig. 4-7: *Temperature Distribution Profile in Fin Sheet at 08:00.*

(2) At 12:00

In the edge, slightly colder due to effect of convection, slowly increasing when moving toward the center, this because we are in the midday were maximum heat gain and accumulation in the system. A sudden drop in the central area owing to the fact that the central line (nodes) of the fin is situated in the area sticking to the evaporation section of the loop heat pipe, where the temperature was at the lowest level due to the evaporative effect of the heat pipe fluid. As a result, the heat flow was directed from the fin's edges to its central line.

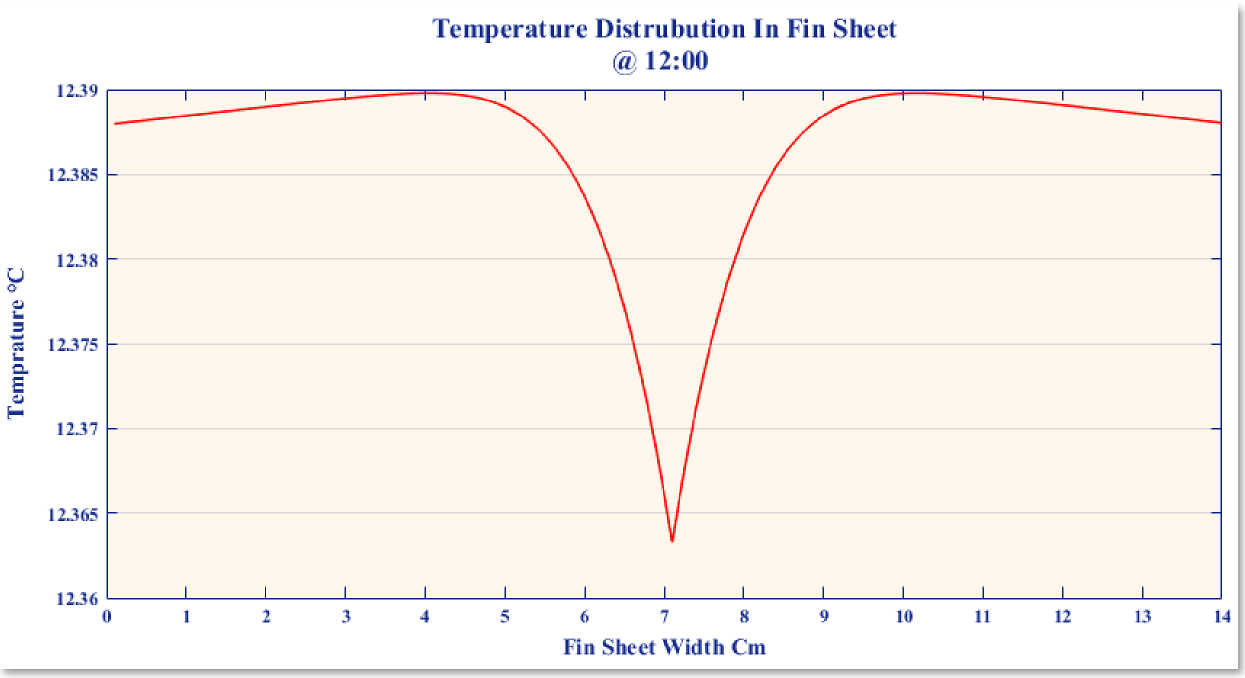

Fig. 4-8: *Temperature Distribution Profile in Fin Sheet at 12:00.*

In **Fig. 4-8** at 12:00 the fast heat gain and accumulation has an influence over the heat pipe heat extraction process

(3) At 16:00

The temperature along the fin sheet is mostly dominated by the LHP heat extraction, but the ambient temperature still in increasing trend and the solar beams incidence still good. The profile is tending to be a V-shape.

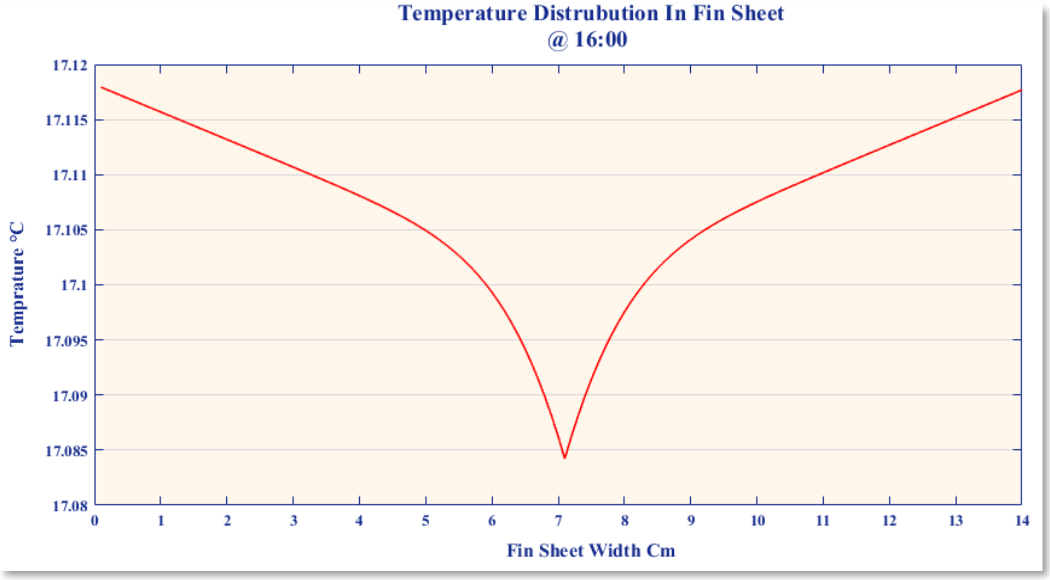

Fig. 4-9: *Temperature Distribution Profile in Fin Sheet at 16:00.*

(4) At End 18:50

The temperature along the fin sheet is dominated by heat pipe. Perfect V-shape is now obtained.

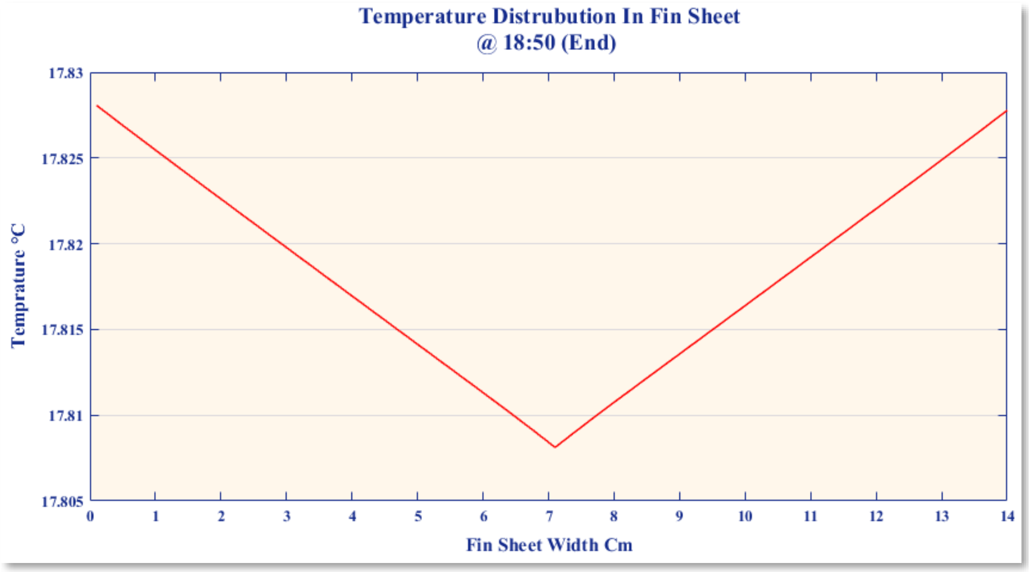

Fig. 4-10: *Temperature Distribution Profile in Fin Sheet at End 18:50.*

(5)3D Temperature Distribution Profile in Fin Sheet

A 3D temperature distribution for the fin sheet against the fin width and the operating time is displayed in **Fig. 4-10**, achieved by running the dynamic simulation model.

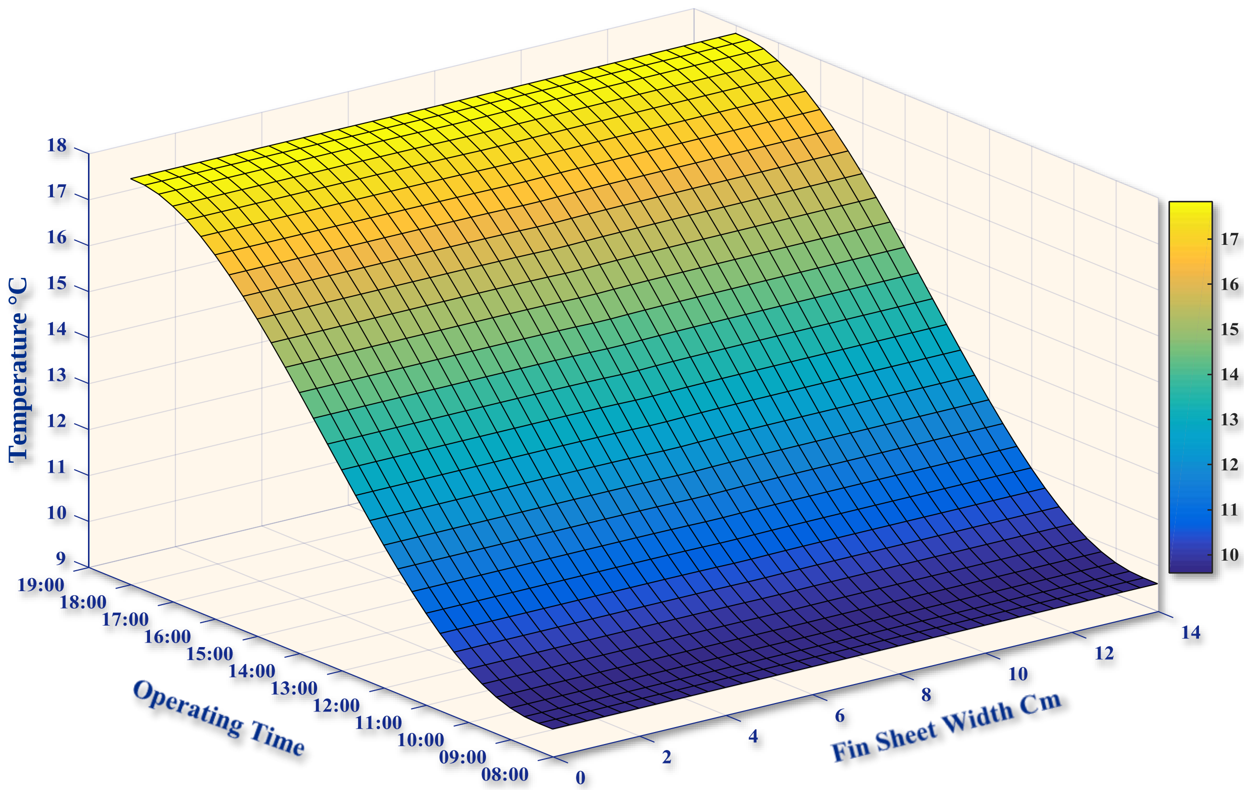

Fig. 4-11: *3D Temperature Distribution Profile in Fin Sheet.*

IV.2.6. Water Heat Gain and Refrigerant Mass Flow Rate

The average water heat gain and the refrigerant mass flow rate were presented in Fig. 4-11. The average water heat gain was 181.33 W. The Qw variation trend was similar to the refrigerant flow rate, a slow up-rising in the morning, max at midday and quick decrease in late afternoon.

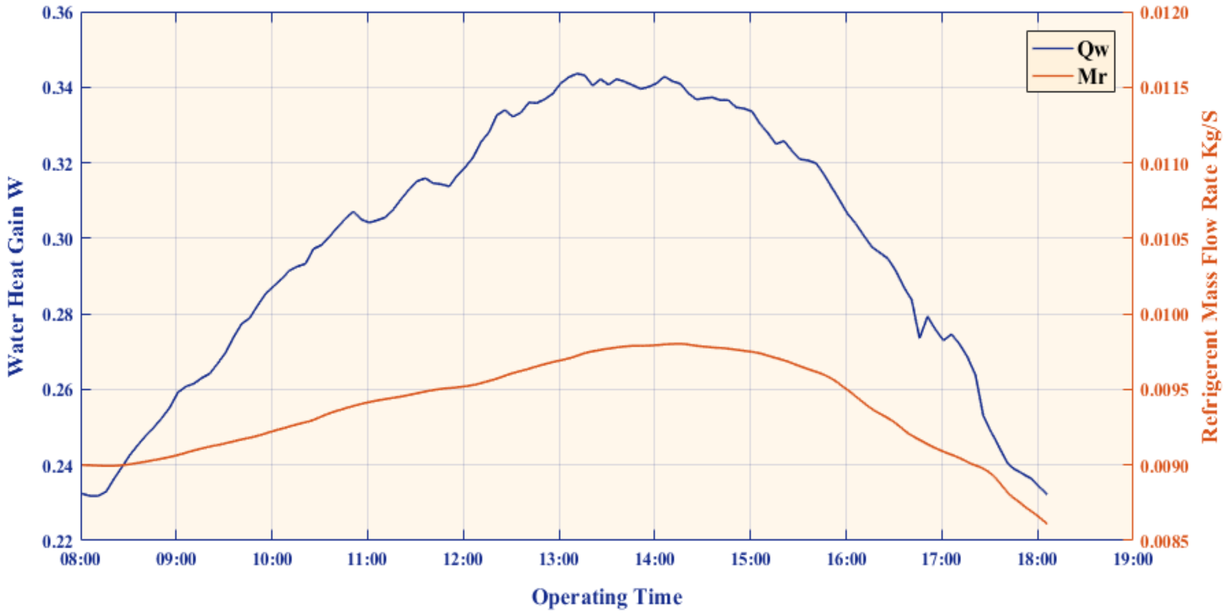

Fig. 4-12: *Water Heat Gain and Refrigerant Mass Flow Rate.*

IV.3. Conclusion

This work investigation into the dynamic performance of a solar photovoltaic/loop-heat-pipe heat pump assisted system, with the potential to overcome persistent difficulties in the existing PV/T technologies. Based on most recent ideas of enhanced PV module thermal conductivity and calculation of optimum tilt angle, a dedicated computer model was developed to predict the system's performance on the basis of the heat balances principle.

The mean daily PV temperature was about 14.1 °C meanwhile the mean ambient temperature was 12.7 °C. The PV layer and the heat pipe wall were matching in the morning and end of day, meanwhile separated slightly during the day reached maximum difference of 0.9 °C at midday, this can be owned to the thermal enhancement of the system. The total efficiency was found to trend oppositely to the PV layer cooling rate, which is a reasonable natural behavior. The water tank was a 35L capacity with a daily in/out rate of 1 m^3, the water temperature continuously increased by nearly 51.1 °C and reached the final temperature over 60.8 °C with an average slope of 4.6 °C/hour.

The average electrical and thermal efficiencies of the PV/LHP module was 11.30% and 53.41% respectively. Instantaneous electrical and thermal outputs and their corresponding efficiencies variation trends were responding and fully coherent with the real climatic operational conditions throughout the day duration, this concluded that the established computer model was able to predict the system's performance with a reasonable accuracy.

This research simulated the dynamic performance of PV/LHP heat pump system under the real climate conditions. A comparison with a similar previous work showed good agreement with reserve of remarkable higher efficiencies from 9.12 to 11.30 % for the electrical and from 38.13 to 53.41% for the thermal. The research results predicted such a good performance enhancement will encourage to build the proposed PV/LHP system and experimentally test it, which in its turn will help develop a high performance solar PV/T system that can contribute to significant fossil fuel energy saving and carbon emission in the building sector.

Bibliography

Bibliography

[1]. Roger A. Messenger, Jerry Ventre. Photovoltaic System Engineering, 2nd ed., Florida (USA): CRC Press; 2003, 54-55.

[2]. Brinkworth et al., Thermal regulation of photovoltaic cladding. Solar Energy 1997; 61:169–78.

[3]. Kranter et al., Combined photovoltaic and solar thermal systems for facade integration and building insulation. Solar Energy 1999; 67: 239–48.

[4]. Kalogirou SA, Tripanagnostopoulos Y. Hybrid PV/T solar systems for domestic hot water and electricity production. Energy Conversion and Management 2006; 47: 3368–82.

[5]. Mustafa Kaya, Thermal and Electrical Performance Evaluation of PV/T Collectors in UAE, May 2013; P 5-10. EGI-2013-037 MSC

[6]. J.A. Duffle, W.A. Beckman, Solar engineering of Thermal Processes, second ed., John Wiley and Sons Inc., New York, 1991.

[8]. Zondag HA, De Vries DW, Van Helden WGJ, Van Zolingen RJC, Van Steenhoven AA, The yield of different combined PV-thermal collector designs, Solar Energy 2003; 74: 253–269.

[9]. X. Zhao, X. Zhang, S. B. Riffat, X Su, Theoretical investigation of a novel PV/e roof module for heat pump operation, Energy Conversion and Management 2011; 52: 603-614.

[10]. Heat pipe, < heatpipe.nl/index.php?page=heatpipe&lang=EN>, [19.11.2010]

[11]. Xingxing Zhang et al. Design, fabrication and experimental study of a solar photovoltaic/loop-heat-pipe based heat pump system, 2013, p 2-17.

[12]. S.C. Solanki, Swapnil Dubey, Arvind Tiwari, Indoor simulation and testing of photovoltaic thermal (PV/T) air collectors, Applied Energy 2009; 86: 2421–2428.

[13]. Huang B. J., Liu T. H., Hung W. C., Sun F. S., Performance evaluation of solar photovoltaic/thermal systems. Solar Energy 2001; 70: 443-448.

[14]. J. Ji et al., Experimental study of photovoltaic solar assisted heat pump system, Solar Energy 2008;82: 43–52.

[15]. Z. Quan, N. Li, Y. Zhao, X. Tang, the experiment research for solar PV/T system based on flat-plate heat pipes, Proceeding the 17th Chinese national HVAC&R academic conference, 2010.

[16]. Hendrie SD. Evaluation of combined photovoltaic thermal collectors. In: ISES international congress and silver jubilee; 1980. p. 1865–1869.

[17]. Cox CH, Raghuraman P. Design considerations for flat-plate photovoltaic/thermal collectors. Sol Energy 1985; 35:227–41.

[18]. Huang BJ. Performance rating method of thermosyphon solar water heaters. Sol Energy 1993; 50:435–40.

[19]. Bergene T, Lovvik OM. Model calculations on a flat plate solar heat collector with integrated solar cells. Sol Energy 1995; 55:453–62.

[20]. Duffle JA, Beckman WA. Solar engineering of thermal processes. 2nd ed. New York, NY: John Wiley and Sons Inc; 1991.

[21]. Garg HP, Agarwal RK. Some aspects of a PVT collector/forced circulation flat plate solar water heater with solar cells. Energy Convers Manage 1995; 36:87–99.

[22]. Sopian KS, Yigit HT, Liu HT, Kakac S, Veziroglu TN. Performance analysis of photovoltaic thermal air heaters. Energy Convers Manage 1996 ; 37:1657–70.

[23]. De Vries DW. Design of a photovoltaic thermal combi-panel. In: PhD report. UT; 1998.

[24]. Zondag HA, De Vries DW, Van Helden WGJ, Van Zolingen RJC, Van Steenhoven AA. The yield of different combined PV–thermal collector designs. Sol Energy 2003; 74:253–69.

[25]. Zondag HA, De Vries DW, Van HeldenWGJ, Van Zolingen RJC, Van Steen hoven AA. The thermal and electrical yield of a PV–thermal collector. Sol Energy 2002; 72:113–28.

[26]. Kalogirou SA. Use of TRYNSYS for modeling and simulation of a hybrid PV– thermal solar system for Cyprus. Renewable Energy 2001; 23:247–60.

[27]. Jones AD, Underwood CP. A thermal model for photovoltaic systems. Sol Energy 2001; 70:349–59.

[28]. Huang BJ, Lin TH, Hung WC, Sun FS. Performance evaluation of solar photovoltaic/thermal systems. Sol Energy 2001; 70:443–8.

[29]. Kalogirou SA, Tripanagnostopoulos Y. Industrial application of PV/T solar energy systems. Appl Therm Eng 2007; 27(8):1259–70.

[30]. Sandnes B, Rekstad J. A photovoltaic thermal (PVT) collector with a polymer absorber plate: experimental study and analytic model. Sol Energy 2002; 72:63–73.

[31]. Sandnes B, Rekstad J. A photovoltaic thermal (PVT) collector with a polymer absorber plate: experimental study and analytic model. Sol Energy 2002; 72:63–73.

[32]. Chow TT. Performance analysis of photovoltaic–thermal collector by explicit dynamic model. Sol Energy 2003; 75:143–52.

[33]. Tiwari A, Sodha MS. Performance evaluation of solar PVT system: an experimental validation. Sol Energy 2006; 80:751–9.

[34]. https://en.wikipedia.org/wiki/Heat_pipe

[35]. Advanced Cooling Technologies: https://www.1-act.com/resources/heat-pipe-fundamentals/heat-pipe-article-1968/

[36]. https://en.wikipedia.org/wiki/Loop_heat_pipe

[37]. Pei Gang et al. A numerical and experimental study on a heat pipe PV/T system; Solar Energy 85 (2011) 911–921

[38]. Xingxing Zhang et al. Design, fabrication and experimental study of a solar photovoltaic/loop-heat-pipe based heat pump system; Solar Energy 97 (2013) 551–568

[39]. Sampan Rittidech et al. A numerical for Predicted Efficiency of a Solar Collector Installed Heat Pipe; Australian Journal of Basic and Applied Sciences 2015; ISSN:1991-8178.

[40]. Tripanagnostopoulos Y. Aspects and improvements of hybrid photovoltaic thermal solar energy systems. Sol Energy 2007; 81:1117–31.

[41]. Tonui JK, Tripanagnostopoulos Y. Performance improvement of PVT solar collectors with natural air flow operation. Sol Energy 2008; 82:1–12.

[42]. Solanki SC, Dubey S, Tiwari A. Indoor simulation and testing of photovoltaic thermal (PVT) air collectors. Appl Energy 2009; 86:2421–8.

[43]. Dubey S, Sandhu GS, Tiwari GN. Analytical expression for electrical efficiency of PVT hybrid air collector. Appl Energy 2009; 86:697–705.

[44]. Ji J, et al. Distributed dynamic modelling and experimental study of PV evaporator in a PVT solar-assisted heat pump. Int J Heat Mass Transfer 2009; 52:1365–11373.

[45]. Shahsavar A, Ameri M. Experimental investigation and modeling of a direct coupled PVT air collector. Sol Energy 2010; 84:1938–58.

[46]. Zhao X, Zhang X, Riffat SB, Su X. Theoretical investigation of a novel PV/e roof module for heat pump operation. Energy Convers Manage 2011; 52:603–14.

[47]. Touafek K, Haddadi M, Malek A. Design and modeling of a photovoltaic thermal collector for domestic air heating and electricity production. Energy Build 2013; 59:21–8.

[48]. Amrizal N, Chemisana D, Rosell JI. Hybrid photovoltaic–thermal solar collectors dynamic modelling. Appl Energy 2013; 101:797–807.

[49]. Bakar NAM, Othman M, Mahadzir HD, Manaf NA, Jarimi H. Design concept and mathematical model of a bi-fluid photovoltaic thermal (PVT) solar collector. Renewable Energy 2014; 67:153–64.

[50]. J. Allan et al. Enhancing the thermal conductivity of ethylene-vinyl acetate (EVA) in a photovoltaic thermal collector; AIP Advances 6, 035011 (2016); doi: 10.1063/1.4944557.

[51]. Operation of Loop Heat Pipes, < china-heatpipe.net/ >.

[52]. Water properties, <www.efunda.com/materials>.

[53]. Water thermal properties, <www.engineeringtoolbox.com>.

[54]. Plate heat exchanger, <en.wikipedia.org/wiki/Plate_heat_exchanger>.

[55]. C. A. Busse, Theory of ultimate heat transfer limit of cylindrical heat pipes, International Journal of Heat and Mass Transfer 1973; 16:169-186.

[56]. S.W. Chi, Heat pipe theory and practice: a source book, Washington: Hemisphere Pub. Corp, 1976.

[57]. Zhao Xiaobao, Analysis and Amendment of Design Factors about Heat Pipe of Screen Wicks, Journal of Nanjing normal University 2004; 04(03): 07-10.

[58]. Imura H, Kozai H, Ikeda Y, The effective pore radius of screen wicks [A], Ma Tongze. Advances in Heat Pipe Science and Technology[C], Proceedings of the 8th International Heat Pipe Conference, 1992: 113-118.

[59]. Kraus AD, Bar-Cohen A. Thermal Analysis and Control of Electronic Equipment. McGraw-Hill, 1983.

[60]. Riffat SB, Zhao X, Doherty PS. Analytical and numerical simulation of the thermal performance of 'mini' gravitational and 'micro' gravitational heat pipes, Applied Thermal Engineering 2002; 22: 1047–1068.

[61]. Vapour-temperature function, <http://en.wikipedia.org/wiki/vapour_pressure_of_water>.

[62]. Xingxing Zhang, investigation of a novel solar photovoltaic/loop-heat-pipe heat pump system 2014, p 97-107.

[63]. W. Rohsenow, J.Hartnet, Y.Cho, Handbook of Heat Transfer, 3rd edition, McGraw-Hill, 1998.

[64]. Soteris A. Kalogirou, Solar energy engineering: process and system, Elsevier Inc., 2009.

[65]. Camelia Stanciu et al. Optimum tilt angle for flat plate collectors all over the World – A declination dependence formula and comparisons of three solar radiation models, Energy Conversion and Management 81 (2014) 133–143

[66]. Klein, S.A, Calculation of flat-plate collector heat-loss coefficients, Solar Energy 1975; 17(01): 79-80.

[67]. Stephen R. Turns, Thermodynamics: concepts and applications, Cambridge University Press, 2006.

[68]. Michael J. Moran, Howard N. Shapiro, Fundamentals of engineering thermodynamics, 3rd edition, John Wiley and Sons Inc., 1995.

[69]. Jianfei Jiang, Liangjian Hu, Jian Tang, Numerical analysis and MATLAB experiment, Siencep press, 2004.